Pacific
Northwest
NATIONAL LABORATORY

Feasibility Study of Advanced Manufacturing Techniques and Compositions of High Entropy Alloys

August 2023

Mohan Sai Kiran Kumar Yadav Nartu
Subhashish Meher
Isabella van Rooyen
Shalini Tripathi
Nathan Canfield

M3CT-23PN1304081

DISCLAIMER

This report was prepared as an account of work sponsored by an agency of the United States Government. Neither the United States Government nor any agency thereof, nor Battelle Memorial Institute, nor any of their employees, makes **any warranty, express or implied, or assumes any legal liability or responsibility for the accuracy, completeness, or usefulness of any information, apparatus, product, or process disclosed, or represents that its use would not infringe privately owned rights**. Reference herein to any specific commercial product, process, or service by trade name, trademark, manufacturer, or otherwise does not necessarily constitute or imply its endorsement, recommendation, or favoring by the United States Government or any agency thereof, or Battelle Memorial Institute. The views and opinions of authors expressed herein do not necessarily state or reflect those of the United States Government or any agency thereof.

Feasibility Study of Advanced Manufacturing Techniques and Compositions of High Entropy Alloys

August 2023

Mohan Sai Kiran Kumar Yadav Nartu
Subhashish Meher
Isabella van Rooyen
Shalini Tripathi
Nathan Canfield

M3CT-23PN1304081

Pacific Northwest National Laboratory
Richland, Washington 99354

Summary

In line with the objectives of Department of Energy's Office of Nuclear Energy Advanced Materials and Manufacturing technologies program (AMMT), this work focuses on new materials development and qualification research and development for next-generation, high-temperature nuclear reactors. While the currently qualified nuclear materials have demonstrated significant irradiation resistance at high temperatures, the community is still interested in materials that can sustain the harsh environments found in nuclear reactors for temperatures up to 1,000°C for nearly 100,000 hours. High entropy alloys (HEAs) have the potential to serve in these extreme environments of next generation nuclear reactors due to their unique phase transformation pathways and nanoscale and mesoscale microstructures. The current work focuses on understanding such nuclear energy relevant HEAs through a detailed literature survey, selected experimental work and developing a decision matrix with criteria for identification of HEAs with may have most impact and value for further examination.

The HEA classification used in this study and the elaborate literature survey performed provide insights into the processing, microstructure, and properties of the several HEAs reported targeting different applications. Six HEAs were identified as promising for the nuclear industry focusing on the high temperature properties with Co as an alloying element in two of these alloys (($Ni_2Co_2FeCr)_{92}Al_4Nb_4$; $Al_{0.3}Ti_{0.2}Co_{0.7}CrFeNi_{1.7}$). GRX-810 (Co-33%, Cr-29%, Re-1.5%, Al-0.3%, Ti-0.25%, Nb-0.75%, W-3%, C-0.05%, Ni-Balance), developed by NASA shows creep performance 2-3 orders of magnitude better than the current high temperature alloys, is best classified as a medium entropy alloy or an oxide dispersion strengthened (ODS) alloy due to the presence of Y_2O_3 particles and therefore, we recommend pursuing this material as part of a different AMMT work package. Although the decision matrix is not fully developed yet for the six candidate HEAs, the literature survey provides technical justification to down select two HEAs ($Al_{0.3}Ti_{0.2}Co_{0.7}CrFeNi_{1.7}$ and $Al_{10}Cr_{12}Fe_{35}Mn_{23}Ni_{20}$) for detailed experimental work. An advanced processing route was evaluated for fabricating functionally graded HEAs using Directed Energy Deposition (DED) and off-the-shelf metal alloy powders. This advanced processing methodology for functionally graded HEAs would open avenues for rapidly assessing new HEA compositions at significantly cheaper costs.

Most of the HEA research reviewed, used arc (73%) and vacuum melting (15%) processes as a fabrication method, with only 11% of the papers reviewed used laser based additive manufactured processes. Solid state manufacturing processes were only reported in less than 5% of the instances. The literature survey shown therefore the opportunity to explore solid phase processes as a manufacturing technique due to the grain refinement and decreased segregation properties during processes. Therefore, the inclusion of Shear Assisted Processing and Extrusion (ShAPE) is in progress for the two down-selected HEAs ($Al_{0.3}Ti_{0.2}Co_{0.7}CrFeNi_{1.7}$ and $Al_{10}Cr_{12}Fe_{35}Mn_{23}Ni_{20}$) due to its unique processing conditions which result in finer microstructures with compositionally homogenous grains that would potentially enhance the mechanical properties. In addition, the effect of solid phase processing on the mechanical properties of a single-phase HEA can also provide valuable information and potential more economical routes to HEA adoption to the markets. It is therefore also recommended that a functional graded alloy to HEA as a final coating be explored to determine the impact on the interlayers and interface properties.

The temperature-dependent (from Room Temperature (RT) to 500°C) nanoindentation behavior of the DED and SLM processed $Al_{0.3}Ti_{0.2}Co_{0.7}CrFeNi_{1.7}$ HEA was investigated in the as-deposited and one-step annealed conditions for this study. The hierarchically heterogeneous

microstructures obtained via simple one-step annealing of the DED and selective laser melting (SLM) -processed HEA exhibited significantly better performance than the nearly homogeneous microstructures in the as-deposited state. The one-step annealed conditions revealed less than 6.6% reduction in hardness values at 500°C compared to RT, while the as-deposited conditions showed greater than 18% reduction in hardness between RT and 500°C. The one-step annealed conditions also exhibited significantly higher hardness than the as-deposited conditions owing to their multi-phase (FCC+$L1_2$) microstructures with a substantial fraction of ordered $L1_2$ precipitates. Furthermore, serrated yielding (Portevin-Le Chatlier (PLC) effect) indicative of microstructural instability was observed during nanoindentation deformation (at 500°C) for both SLM and DED processed conditions but not after the one-step annealing. Overall, the nanoindentation results signify the stability of these hierarchically heterogeneous microstructures developed via single step annealing, exploiting the residual stresses, in the Additively Manufactured $Al_{0.3}Ti_{0.2}Co_{0.7}CrFeNi_{1.7}$ HEA. Overall, the results presented were promising. However, applying this HEA in high-temperature nuclear reactors would require a more detailed assessment of other properties. ShAPE processing followed by high-temperature, nano-indentation testing at 800°C is in progress. This HEA is also expected to have high-temperature stability up to ~1100 °C.

Microstructural characterization of the graded compositions of HEAs fabricated via DED technique using off-the-shelf common alloy powders has been performed. The results reveal homogenous compositions in each build layer. However, the graded HEAs formed dendritic-interdendritic microstructures mainly due to the presence of heavier elements, such as Nb. Few regions contained unmelted 316 L powders with nano-scale Cr rich precipitates sparsely distributed. Additionally, Ti-oxide particles were observed in the HEA matrix. While the microstructural examination indicates the successful fabrication of graded materials, further investigation is needed to optimize the process parameters to reduce porosity and undesired brittle intermetallic phases and ensure complete melting of the metal alloy powders.

The collaboratively determined decision matrix is briefly discussed with a preliminary rating of selected HEAs. It should however be noted that the finalization of the ratings in the decision matrix will continue, as the full battery of experimental work is in process that may influence the final decision based on the determined rating. HEA $Al_{10}Cr_{12}Fe_{35}Mn_{23}Ni_{20}$ performed marginally better than HEA $Al_{0.3}Ti_{0.2}Co_{0.7}CrFeNi_{1.7}$ with a rating of 62.5 vs 56.5.

The research performed as part of this study, resulted in three conference presentations and one accepted journal publication.

Acknowledgments

Acronyms and Abbreviations

AD	As-deposited
AM	Additive manufacturing
AMMT	Advanced Materials and Manufacturing Technology
BCC	Body centered cubic
DED	Directed energy deposition
EBAM	Electron beam additive manufacturing
FCC	Face centered cubic
FIB	Focused ion beam
FY	Fiscal year
GB	Grain boundary
HCP	Hexagonal close packed
HEA	High entropy alloy
HIP	Hot isostatic pressing
LANL	Los Alamos National Laboratory
LENS	Laser engineered net shaping
LPBF	Laser powder bed fusion
ORNL	Oakridge National Laboratory
ODS	Oxide dispersion strengthened
PNNL	Pacific Northwest National Laboratory
PLC	Portevin-Le Chatlier
RHEA	Refractory high entropy alloy
RT	Room Temperature
SEBM	Selective electron beam melting
SEM	Scanning electron microscopy
ShAPE	Shear Assisted Processing and Extrusion
SLM	Selective laser melting
SS	Stainless steel
STEM	Scanning TEM
SPS	Spark plasma sintering
TEM	Transmission electron microscopy
TRIP	Transformation induced plasticity
TWIP	Twinning induced plasticity
UTS	Ultimate tensile strength
VLM	Vacuum levitation melting
WAAM	Wire arc additive manufacturing
XRD	X-ray diffraction

YS   Yield Strength

Contents

Figures

Tables

1.0   Introduction

The AMMT Program is to develop cross-cutting technologies in support of a broad range of nuclear reactor technologies, and to maintain U.S. leadership in materials and manufacturing technologies for nuclear energy applications. The overarching vision of the AMMT program is to accelerate the development, qualification, demonstration and deployment of advanced materials and manufacturing technologies to enable reliable and economical nuclear energy. Through advanced manufacturing techniques, new materials can be created for many applications in nuclear reactors. These materials can further the development of advanced reactors where properties such as improved high temperature strength, improved corrosion resistance or improved radiation tolerance are needed. Achieving this, can provide a safety improvement through larger safety margins, economic benefit for higher efficiency during operation and a cost reduction through more cost-effective manufacturing processes and less waste.

1.1   Background

In recent times, there has been significant effort in developing new structural materials, such as bulk metallic glasses [1 – 4], oxide dispersion strengthened (ODS) steels [5 – 7], ceramics [8 – 12], nano-layered composites [13 – 17], and high entropy alloys (HEAs) [18] for next-generation nuclear reactor applications. The AMMT program initiated a multi-lab effort by Oakridge National Laboratory (ORNL) (work package CT-23OR130406), Los Alamos National Laboratory (LANL) (work package CT-23LA130403) and Pacific Northwest National Laboratory (PNNL) (work package CT-23PN130408) to evaluate and focus on the advanced manufacturing techniques applied for new material development of ODS nuclear materials, refractory composites, and alloys, and HEAs, respectively. By performing this work, the opportunity is created to explore the recent advances in these material groups, due to the promise of high temperature performance, corrosion, and irradiation tolerance. In addition to specific microstructural challenges for each material group, the need for upscaled manufacturing techniques is still one of the biggest hurdles in advancing the TRL of these material groups. The execution of this multi-lab effort research will provide the AMMT program a merit-based feasibility study identifying an accelerated development path for these materials. This merit-based decision matrix was developed through collaboration of ORNL, LANL and PNNL. A comparison between these three material types will be made during the next phase of this work and will be collaboratively reported in the September 2023 M2 milestone (Preliminary feasibility studies of new materials for advanced manufacturing) led by ORNL.

Structural materials need to sustain against creep and void swelling and exhibit reasonably high mechanical strength and fracture toughness under irradiation at high temperatures (>300°C). There are commonly three main strategies for improving the radiation tolerance in materials: (a) Designing radiation-resistant matrix phases; (b) Immobilizing the vacancies and interstitials; and (c) Enhancing the sink strength of the material [19]. Among the new materials, HEAs are shown to address all three design strategies [1] and thus form an integral part of the advanced materials development portfolio and a reason for further exploration under the current work package.

HEAs with significantly higher configurational entropy than conventional alloys exhibit unusual lattice distortion and sluggish diffusion, which could potentially immobilize the radiation-induced defects and result in undesired swelling and segregation; this is detrimental to mechanical and functional properties[2–10]. The high levels of transmutation in conventional alloys may already produce compositionally complex alloys locally resembling HEAs [1,11,12].

While the first two strategies (a) and (b) mentioned previously can only augment the radiation resistance of the HEAs to a limited extent, the third strategy, (c) enhancing the sink strength of the material, can show multifold improvement in the radiation resistance [13–15]. One of the ways to improve the sink strength of the HEAs is to have multiple interfaces either by secondary phase precipitation or by a multi-modal distribution of grain sizes, including nano-structured grains. HEAs offer significant potential for inducing such microstructural heterogeneities, but conventional casting is tedious and time-consuming [13,16–18]. For instance, the microstructure of a transformation induced plasticity (TRIP)-enabled HEA has been innovatively engineered by Agrawal et. al., for enhanced radiation resistance [13]. The processing route involved a preliminary homogenization annealing of the cast HEA followed by a hot rolling to eliminate the cast defects. The rolled HEA was eventually descaled, heat treated at 500°C (desired phase field), and then warm-rolled to obtain a massively interfaced alloy.

Considering this, AM methods like DED and [19–22]SLM can be beneficial, as materials with significantly better properties than the conventionally cast counterparts can be obtained[23–27]. Moreover, straightforward one-step annealing approaches can be designed by exploiting the residual stresses in these AM techniques to successfully engineer microstructures with multiple interfaces desired for nuclear applications[28,29]. The DED process can also enable the fabrication of functionally graded materials that possess applications across different industries, including nuclear. Additionally, the functionally graded materials produced via DED can rapidly assess the material's properties [19–22,30–33], reducing the overall cost of down selecting in a given compositional space, especially HEAs [34,35]. ShAPE is another recently developed solid-state processing technique that produces parts with significantly finer and compositionally homogenous microstructures that result in enhanced functional and mechanical properties [36]. Therefore, it is worthwhile for the nuclear industry to investigate novel high-entropy alloys via advanced manufacturing processes.

1.2 PNNL HEA work scope and objectives

The overall objective of the PNNL HEA work scope is to evaluate the current manufacturing techniques applied for HEAs, addressing challenges and needs for upscaling the current manufacturing processes, and to identify HEAs relevant to the nuclear industry. To reach this goal, the specific work scope is shown in Figure 1 and includes:

(1) A comprehensive literature survey of current manufacturing techniques applied for HEAs and the current HEAs explored in research communities; and identifying HEAs relevant specifically for nuclear applications.

(2) Characterization and property measurement of down select of HEA compositions to aid decision making criteria.

(3) Bulk manufacturing experiments using both liquid and solid-state manufacturing processes to determine the effectiveness of advanced techniques.

(4) Finally, all information will be contributing towards the completion of the decision matrix for HEAs for nuclear application with recommendations for future work to increase the technical readiness of bulk HEAs.
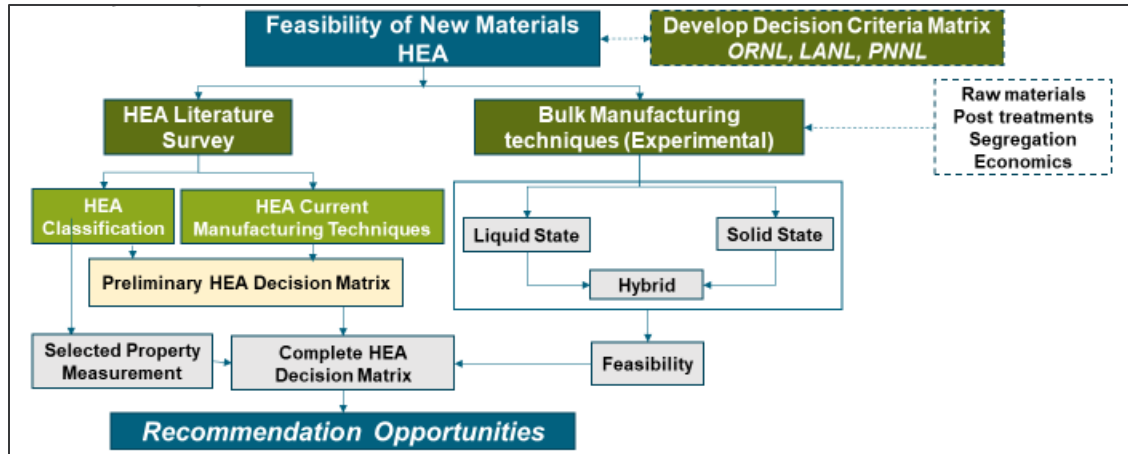
Figure 1: PNNL work scope includes literature survey and experimental work.

1.3 Report Content

This report provides a comprehensive summary of the current HEA literature pertaining manufacturing methods used for research studies, the HEA classification (type) and selected characterization and property measurements. The collaboratively determined decision matrix is briefly discussed with a preliminary rating of selected HEAs. It should however be noted that the finalization of the decision matrix will continue, as the full battery of experimental work is in process (due to projects start date due to funds availability) that may influence the final decision based on the rating. Finally, an outlook of the work to follow is provided with preliminary conclusions based on the work performed to date.

2.0 Decision Criteria Matrix

Creating an objective decision criteria matrix for diverse new materials is challenging, especially considering the wide range of compositionally different materials that can be created. Moreover, certain materials like ODS alloys require unique and sophisticated processing routes; therefore, new criteria reflecting such complexities must be incorporated into the decision criteria matrix. A decision criteria matrix is developed in collaboration with ORNL and LANL and is presented in Table 1. This decision criteria matrix for new and diverse materials will be used to evaluate the potential of HEAs for nuclear reactor applications.

Table 1:Decision Criteria Matrix

Category	Criteria	What is being evaluated?	Notes
Application Space	Applicability to different reactor types	Whether a material can be used in multiple types of reactors or not.	
	Other Industry Experience	The interest in and use of a material by other industries.	
	Data Availability	The availability and comprehensiveness of data associated with a given material.	Pertinent data includes radiation resistance, elemental transmutation, high temperature oxidation, SCC, thermal performance, creep, fatigue, tensile properties, etc.
	Code and Standards Availability	The availability of codes and standards which govern the production, material quality/standards, and implementation of a material.	Technically six areas (codes*3+standards*3) - facets of material implementation
	Component Versatility	The potential for a material to be used for different types of components in a nuclear reactor or power plant.	The types of components include cladding, in-core structural, out of core structural, and balance of plant component.
Environmental Compatibility	Radiation Resistance	The ability of a material to maintain its shape, size, and properties after exposure to radiation.	Evaluating things like a material's resistance to swelling, void formation, and embrittlement
	Elemental Transmutation	Elemental stability of a material and impact of transmutation.	Does the material transmute to a undesirable element with detrimental properties? Does the material become activated leading to increased dose?

	High-Temperature Oxidation Resistance	The ability of a material to resist oxidation at high temperatures.	It would perhaps be ideal to specify an oxidation rate (mm hr^{-1}, or g cm^{-2} hr^{-1}), but this will inevitably vary with temperature. Possibly a normalization of temperature could address this.
	Neutronics Compatibility	The degree to which a material impacts the neutron economy of reactors.	Zr thermal capture cross section ~2 b, fast capture cross section ~10e-2 b
	Coolant Compatibility and Corrosion Resistance	The relative stability and compatibility of a material in coolants used in the next generation of reactors, including its resistance to corrosion, erosion, and other chemical reactions.	Types of coolants include water (normal or SC), gas (CO_2, He), liquid metals (Pb, Pb-Bi, Na, NaK), and molten salts (FLiBe).
Physical and Mechanical Properties	Thermal Conductivity	Capability of a material (with high thermal conductivity) to increase the thermal efficiency of an energy system and reduce transitional thermal stress in the components	
	Thermal Capacity	General thermal capacity, such as melting point, softening point, and phase stability across temperature range.	Considered steels in fast reactors at ~0.5 T_M
	Tensile Properties	High-temperature tensile properties, including strength, ductility, and type of failure.	Tensile strength and ductility can represent many other relevant properties, such as fatigue limit, fracture toughness, irradiation resistance etc.
	Creep Performance	Risk of losing dimensional stability in long-term service.	Operation temperatures in most reactors will be well below the temperatures where creep mechanisms become active.
	Fatigue	Risk of component failure due to crack growth by cyclic loading.	New candidate materials are general high strength materials and components might be designed to be operated below their fatigue limits.
	Fracture Toughness	Capability to avoid the most probable failure mode with aging and degradation.	Most nanostructured and refractory materials have high crack sensitivity, but it has been ignored.

Microstructure Dependency	The sensitivity of a material's properties to its microstructure.	If we make the material wrong, it fails. Need a high degree of expertise in materials selection and design.
Scope for Microstructural Enhancement	The possibility of enhancing material properties by microstructural engineering through feasible processing routes.	We can enhance the microstructure to improve properties.

Manufacturability

Reproducibility/ Consistency	How reproducibly and consistently the manufacturing route for a material can fabricate components from that material.	Key factor: number of process variables that need to be carefully monitored. Highest score will be assigned to processing techniques which produces consistent microstructures and properties irrespective of the feedstock.
Process Complexity	The number of processing steps required to produce a component from a given material.	Post and preprocessing treatment (thermomechanical treatment, surface finishing, machining). At times, this metric can change drastically based on the type of alloys, for instance ODS alloys needing additional preprocessing will be assigned lower score irrespective of the manufacturing route employed
Cost	Relative overall cost for production of components from a given material.	Considering the costs of the raw material, labor, and fabrication including post processing. We may want to assume the final part is inevitably complex for comparison purpose
Scalability	The ability to increase the overall number of components being produced with a certain material and the ability to produce dimensionally larger components.	Production volume and dimensional: any scale could be chosen based on the application, for the most part, production volume is considered
Production Method Technology Readiness Level	The technology readiness level of common production methods used to produce components from a material.	
Raw Material Supply	Precursor availability in the United States.	Depending on the type of the process considered, the raw material supply rank must change.
Flexibility of Manufacturing	Number of methods which can be used to manufacture material.	If a material type can potentially be manufactured via all the available

		techniques irrespective of whether it has been done or not will be given a 5
Conventional Machining	The ability and need to drill, cut, or otherwise subtract material; perform bending, milling, or use computer numerical control; or use joining techniques (such as welding) to manufacture a component from the given material.	It is the ability to manufacture a full component using the considered processing technique
Near Net Shaping (Complexity of Shape)	The availability of manufacturing routes to form near net shape components from a material and the degree of complexity of that shape.	AM will be given five and conventional casting techniques will be ranked lower

3.0 Literature Survey on High Entropy Alloys

This section defines HEAs, current manufacturing techniques applied during research and provide the classification of alloys with the review of alloy compositions with the summarized properties observed.

3.1 What are HEAs?

HEAs are defined as alloys with five or more principal elements. The concentration of each principal element is 5 – 35% [37]. In addition to the principal elements, HEAs may contain other elements in minor quantities, below 5 atomic %. The entropy of mixing multiple principal elements is much more pronounced in HEAs than conventional alloys, which possibly facilitates the formation of solid solution phases with less complicated crystal structures as compared to the conventional alloys. However, presence of multi-principal elements of different groups increases the propensity for formation of multi-phase microstructures in HEAs. The high mechanical strength [38], exceptional wear resistance [39], good high temperature properties [40], and outstanding corrosion and oxidation resistance[41,42] are commonly observed in HEAs due to their unique multi-principal element compositions.

3.2 Current Fabrication Techniques used for HEAs

The current state of art fabrication techniques that are employed to fabricate HEAs to date are discussed below.

3.2.1 Solid-State Processing

This route includes a preliminary step for producing (via atomization or high energy ball milling) either pre-alloyed HEA powders or individual elemental powders which are later mixed using a ball-mill or roller mixers to obtain the desired HEA compositions.

3.2.1.1 Cold Uniaxial Pressing and Sintering

The mixed/pre-alloyed HEA powders are filled inside a die (typically made of tool steel, H13 steel, EN steel) and cold pressed by two punches (from top and bottom) for a green compact. This green compact is then sintered below melting point to achieve a dense compact [43,44].

3.2.1.2 Hot Pressing

Hot pressing combines both cold pressing and sintering into single step. Since, axial loads are applied on the heated powders so that high density compacts can be obtained[45–47]. An advanced hot pressing, known as hot isostatic pressing (HIP) is also available for compacting HEA powders[48].

3.2.1.3 Spark Plasma Sintering

Spark plasma sintering (SPS) is an advanced sintering process that is also known as pulsed electric current sintering, and which is used to compact powders significantly faster than the conventional sintering process. The fewer procedural steps make this process cost, time, and energy efficient. Further, high density parts with limited grain growth can be obtained in this process [49–52].

3.2.1.4 ShAPE/Friction Stir Additive Processing

Friction stir additive processing is a cost-effective deformation-based processing method that has recently been utilized to fabricate HEAs [53]. ShAPE is a novel technology that can potentially manufacture HEA tubes directly from powders. While HEAs have not yet been processed using this technology, Al alloy tubes with significantly higher densities have been processed from the gas-atomized pre-alloyed powders using this technique [36].

3.2.2 Conventional Liquid State Processing

HEAs are commercially manufactured through melting and casting techniques. One of the main drawbacks of the liquid state processing techniques is the evaporation of the low-melting elements. Further, the slow cooling rates lead to the formation of dendritic/heterogenic microstructures, thereby requiring a post fabrication homogenization heat treatment prior to the application [54,55].

3.2.2.1 Arc Melting Process

Bulk ingots with higher densities (close to the theoretical density) can be produced via arc melting. Another advantage of the arc melting process is the low energy consumption. However, as mentioned above, arc melting produces undesired heterogenous microstructures[54].

3.2.2.2 Vacuum Induction Melting Process[56,57]

The only difference between arc melting and vacuum induction melting) is that the vacuum induction melting involves heating via electromagnetic induction as opposed to electric arc in the arc melting process. The heating and cooling rates can be accurately controlled for nearly homogenous microstructures in this process as compared to the arc melting process [58–60]. One of the main disadvantages of this method is poor surface finish of the solidified products which may need post processing in some cases.

3.2.2.3 Vacuum Levitation Melting Process

The vacuum levitation melting (VLM) is a novel induction melting furnace where the raw metals are levitated in a crucible and alloyed by convective mixing by stirring while under a levitating force. VLM eliminates the contamination from the crucible, and the ingot retains a more uniform microstructure than when using the traditional arc-melting technique [61–64].

3.2.2.4 Directional Solidification Process

In directional solidification process the melt is solidified along a narrow passage in a constrained manner to promote columnar grains, identical grain boundaries, and homogeneous microstructures. This process may even be employed after arc melting/vacuum induction melting to obtain uniformly columnar microstructures for specific applications [15,65]. The processing parameters, such as downward velocity, is shown to impact the yield strength (YS) of the product and thus can be tuned for enhanced mechanical performance [66].

3.2.2.5 Infiltration Process

The infiltration process falls under the category of squeeze casting and has the advantage of producing complex shaped components with relatively lower porosities. This process has mainly been employed to fabricate HEA-oxide composites [67].

3.2.2.6 Electromagnetic Stirring

Electromagnetic stirring process can produce high-quality ingots with minimal defects and porosity [68,69]. It is achieved by placing the magnetic field coils (electromagnetic stirrer) surrounding the crucibles containing the conducting metals/alloy melt. Three different stirring modes: vertical, horizontal, and helical, can be attained by controlling the electromagnetic field strengths [70].

3.2.3 Liquid State Additive Manufacturing

In addition to the typical advantages, such as design freedom, direct implementation of monolithic structures, eliminating the need for riveting/welding/joining and post processing, minimal failure risk, low wastage, etc., the AM processing also results in alloys with superior mechanical properties when compared to the conventionally processed counterparts [23,24,71,72]. Several different AM techniques are available for fabricating HEAs; however, powder bed fusion and DED are the most widely used techniques for manufacturing HEAs.

3.2.3.1 Powder Bed Fusion

Powder bed fusion techniques include SLM and selective electron beam melting (SEBM). In powder bed fusion, parts are printed on a powder bed with substrate underneath. The supporting effect of powder enables printing of complex structures, such as cantilever, hollow, and complex arrays. The parts manufactured by SLM and SEBM exhibit very high dimensional accuracy with negligible surface roughness. While the SLM equipment is simple and works in an argon environment, the SEBM equipment is quite sophisticated and needs a vacuum environment [73–76]. In most cases, the powder bed in the SEBM is heated to avoid charging due to electron beam, which reduces the cooling rates. On the other hand, cooling rates of up to $10^4 – 10^5 K s^{-1}$ can be achieved in SLM as opposed to less than 100 Ks^{-1} in the conventional casting techniques. Thus, parts with significantly finer grain and sub-grain features [77,78] and enhanced mechanical properties can be produced via SLM [79].

3.2.3.2 Directed Energy Deposition

Laser engineered net shaping (LENS[24,28]), wire arc additive manufacturing (WAAM) [80–83], and electron beam additive manufacturing (EBAM) are the most popular DED techniques used for processing HEAs. While LENS is a powder-fed technique, WAAM and EBAM are wire-fed techniques. Also, LENS utilizes a laser beam in contrast to electron beam in EBAM and electric arc in WAAM. The DED techniques typically produce parts with poor surface finish, low dimensional accuracies, and low design complexities compared to the powder bed fusion techniques. However, most DED processed HEAs exhibit better mechanical properties than the conventionally cast counter parts.

3.3 Classification of HEAs

HEAs can be classified based on phase stability and mode of deformation; stable HEAs deform via dislocation slip and metastable HEAs via TRIP and/or twinning induced plasticity (TWIP) upon mechanical/thermal damage. Stable HEAs can be further classified based on the type of phases that constitute the microstructure (See Figure 2 for classification). Moreover, the scope for application of HEAs across various industries is determined mainly by the mechanical properties and secondly by the mode of deformation which forms the basis for this classification. A detailed literature review on HEAs summarizing different aspects such as the microstructure, phase constitution, primary and post processing methods employed, including a summary of findings reported in the articles, is presented in Sections 3.4 and 3.5.
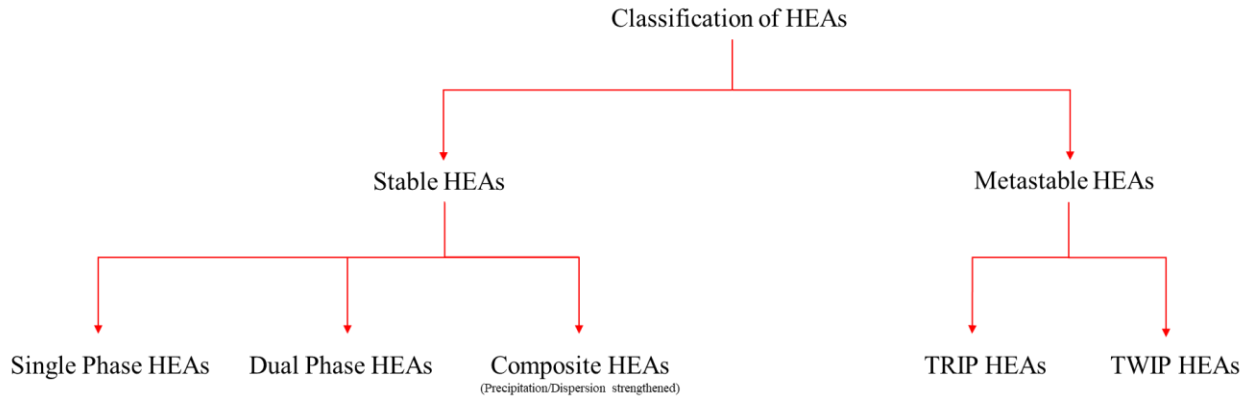
Figure 2: Classification of HEAs

3.4 Stable HEAs

Stable HEAs are further classified as single phase-, dual phase-, and composite HEAs and are discussed:

3.4.1   Single Phase HEAs

A total of 75 single phase HEAs were reviewed, and the summary is presented in Table 2. Out of the 75 HEAs listed below, 61 were manufactured via Arc Melting, 6 were manufactured via Laser Additive Manufacturing Methods, 2 via SPS and 5 via Vacuum Induction Melting and other processes.

Table 2: Literature review on various single-phase HEAs

Composition	Phases	Primary Processing Method	Post Processing Method	Comments
$Al_{0.3}CoCrCu_{0.3}FeNi$	*fcc*	Arc Melting	Homogenized at 1,100℃ for 6 hours followed by annealing	Fundamental understanding of recrystallization kinetics, Al addition to improve
CoCrFeMnNi	*fcc*			

Alloy	Phase	Processing	Heat Treatment	Notes
$Al_{0.2}CoCrFeMnNi$	*fcc*		heat treatment at 900 – 1,100℃ for 1 hour.	solid solution strengthening [84]
AlCoCrFeMn	*Body centered cubic (bcc)*	Arc Melting	None	Al-dependent phase stability; first principles prediction [85]
AlCoCrFeNi	*bcc*	Arc Melting	None	Magnetocaloric values are comparable to Fe-based metallic glasses, such as Fe-Tm-B-Nb and Fe-Zr-B-Co alloys, with a similar transition near RT [86]
$Al_{0.3}CoCrFeNi$	*fcc*	Arc melting/floating [87] zone method/single crystal [88]	Homogenized at 1,250°C	Fundamental study on deformation mechanisms
$Al_{0.3}CoCrFeNi$	*fcc*	Directed energy deposition	None	Better mechanical properties than conventionally processed counterpart [24]
$Al_{0.3}CoCrFeNi$	*fcc*	Selective Laser Melting	None	Significantly better mechanical properties than conventionally processed counterpart [89]
$Al_{0.5}Co_{1.5}CrFeNi_{1.5}$	*fcc*	Arc Melting	Homogenized at a temperature of 1,150°C for 6 hours	The heterogeneous microstructure containing multiple length scales of B2 ppts results in a 400% increase in yield stress when compared to the single-phase FCC condition [90]
$Al_{0.5}CoCrFeNi_{0.5}$	*bcc*	Arc Melting	None	Pressure induced phase transformations from BCC/FCC to hexagonal close packed (hcp) [91]
$Al_{0.25}CoCrFeNi_{0.75}$	*fcc*			
AlCoCrFeNiV	*B2*	Arc Melting	None	High-temperature *in situ* X-ray diffraction in the range of 25 – 800°C[92]
$Al(Co_{0.2}Cu_{0.2}Fe_{0.2}Mn_{0.2}Ni_{0.2})$	*B2*	SPS	Homogenized at 1,100℃ for 10 hours	Single phase intermetallic Improved hardness and low thermal conductivities [93]
$Al(Co_{0.25}Cu_{0.25}Fe_{0.25}Ni_{0.25})$				

AlCoFeNiSm$_{0.1}$TiV$_{0.9}$ AlCoFeNiSm$_{0.1}$V$_{0.9}$	*fcc*	Selective Laser Melting	None	Excellent corrosion resistance and hardness [94]
Al$_{0.075}$Cr$_{0.06}$Fe$_{0.404}$Mn$_{0.348}$Ni$_{0.113}$ + 1.1 at% C	*fcc*	Arc Melting	None	Substantial increase in strength, but also an increase in ductility and work-hardening rate [95]
Co$_{1.7}$CrCu$_{0.1}$FeMo$_{0.3}$Ni CoCrCu$_{0.1}$Fe$_{1.7}$Mo$_{0.3}$Ni CoCrCu$_{0.1}$FeMo$_{0.3}$Ni$_{1.7}$	*fcc*	Arc Melting	None	Phase selection studies based on atomic radius ratio, valence electron concentration, mixing entropy ΔS [96]
CoCrFeMn	*fcc*	Arc Melting	None	Fundamental studies [97]
Co$_{0.10}$Cr$_{0.15}$Fe$_{0.35}$Mn$_{0.05}$Ni$_{0.25}$V$_{0.10}$	*fcc*	Vacuum Induction Melting	homogenized at 1100°C for 6 h followed by cold rolling (~70%) and then annealed above 900°C	Improved cryogenic mechanical properties [98]
CrFeCoNiPd	*fcc*	Arc Melting	None	Significantly higher strength and strain hardenability compared to CoCrFeMnNi- increased stacking fault energy [99]
CoCrMnNi	*fcc*	Arc Melting	None	Binary Gibbs free energy to design HEAs: fundamental study [100]
Co$_{10}$Cu$_{20}$Mn$_{30}$Ni$_{40}$	*fcc*	Vacuum Induction Melting	Homogenized at 1,100°C for 6 hours followed by cold rolling (~70%) and then annealed above 600°C	First Cu-based single-phase HEA designed by Thermocalc; improved cryogenic mechanical properties via grain refinement [101]
CoFeMnNi CoCrFeNi FeNiCoMn NiCoCrMn FeNiCo	*fcc*	Arc Melting	Homogenized at 1,100 – 1,200°C for 24 hours	CoCrNi is the hardest of all the alloys in this series [102]

Composition	Structure	Processing	Post-processing	Notes
FeNiCr				
FeNiMn				
NiCoCr				
NiCoMn				
FeCoNi	fcc	Directed Energy Deposition	None	Higher YS than conventionally processed counterpart [23]
CuIrNiPdPtRh	fcc	Arc Melting	Annealed at 1,400°C for 2 hours	Compressive strength of 1,839 MPa[103]
$Cu_2MnNiZn$ $Cu_2MnNiSn_{0.2}Zn$	fcc	Metallic Mold Casting	None	Brass HEAs: addition of Sn to Cu2ZnMnNi brass HEA reduced the ductility despite the significant hardening of the ingots [104]
$Fe_{0.267}Ga_{0.156}Mn_{0.20}Ni_{0.267}Si_{0.11}$	bcc	Arc Melting	Annealed at 973°C	HEA without rare earths: alloy design based on literature studies [105]
TiZrHfNb	bcc	Directed Energy Deposition	None	TiZrHfNb RHEA exhibits a tensile YS of ~1034 MPa and ductility of ~18.5% at RT.
$TiZrHfNb_{0.8}$	bcc	Directed Energy Deposition	None	Furthermore, for the TiZrHfNb RHEA listed here, the high tensile YS mainly originates from the solid solution strengthening, and the large ductility results from the multiple dislocation interactions promoted by the local chemical fluctuations [106]
$Ti_{40}Zr_{25}Nb_{25}Ta_{10}$				YS ~910MPa ultimate tensile strength (UTS)~1040 MPa
$Ti_{45}Zr_{25}Nb_{25}Ta_5$	bcc	Arc Melting	None	YS ~790 MPa UTS ~910 MPa High corrosion resistance and good biocompatibility [107]
DyErGdHoTb	hcp	Arc Melting	None	Rare-earth HEA with giant magnetocaloric effect [108]

Alloy	Structure	Process	Treatment	Notes
DyErGdHoLuScTbY	*hcp*	Arc Melting	None	To explore the magnetocaloric effect [109]
DyGdHoLaTbY	*hcp*	Arc Melting	None	
DyGdHoTbY	*hcp*	Vacuum Induction Melting	None	Fundamental study: observation of single phase [110]
DyGdLuTbTm	*hcp*	Arc Melting	Annealed at 1173 K	Thermodynamic data from binary phase diagrams to design single-phase HEAs [111]
DyGdLuTbY	*hcp*	Arc Melting	None	
ErGdHoLaTbY	*hcp*	Arc Melting	None	To explore the magnetocaloric effect [112]
GdHoLaTbY	*hcp*	Arc Melting	None	The strengthening effect from the configurational entropy is not found in the alloy [113]
$Al_0/Al_{0.25}/Al_{0.5}/Al_{0.75}/Al_1/Al_{1.5}$ NbTiMoV	*bcc*	Arc Melting	None	Al0.5NbTiMoV has the highest YS (1,625 MPa): high melting, low weight criteria [114]
$Al_{0.4}Hf_{0.6}NbTaTiZr$	*bcc*	Arc Melting	HIPed at 1,200 °C and 207 MPa for 2 h and then annealed at 1,200°C for 24 hours	Complete substitution of Cr with Al in the $CrMo_{0.5}NbTa_{0.5}TiZr$ alloy reduced the alloy density by 10.1%, increased RT hardness and YS by ~12%. Noticeably improved RT ductility and considerably increased, by more than 50%, high-temperature strength in the temperature range from1,073K to 1,473K [115]
$(NiCoCr)_{92}Al_6Ta_2$	*fcc*	Arc Melting	Homogenization treatment at 1,225°C for 24 hours followed by cold rolled to sheet thickness reduction of 70%. Cold-rolled sheets rapidly heated to 1,150°C within ~20 s and dwelled for 3 min.	Testing temperature from 298 K down to 77 K, the YS, ultimate strength, and tensile ductility are increased from ~600 to ~800 MPa, from ~1.0 to ~1.35 GPa and from ~52% to ~90% [116]

NbTiVZr	*bcc*	Arc Melting	HIPed at 1,200℃ and 207 MPa for 2 hours and then annealed at 1,200°C for 24 hours.	At 1,273K, this HEA had 58 MPa strength [117]
MoCrTiAl	*bcc*	Arc Melting	Homogenized at 1,200°C for 24 hours [118].	
NbMoCrTiAl	*bcc*	Arc Melting	Homogenized at 1,300°C for 24 hours	High creep and oxidation resistance:
NbMoTiAl	*bcc*	Arc Melting	Homogenized at 1,500°C for 24 hours	Fundamental studies on phase stability [118]
TaMoCrTiAl	*bcc*	Arc Melting	Homogenized at 1,500°C for 24 hours	
Al$_x$ (HfNbTiZr)$_{100-x}$ (x = 0, 3, 5, 7, 10 and12 in atomic percent)	*bcc*	Arc Melting	Annealed at 1,000°C for 30 minutes	All the HEAs were stable at 1,273K. Al$_5$(HfNbTiZr)$_{95}$ exhibits the excellent RT mechanical properties with combination of fracture strength and elongation of 915.2 MPa and 31.5%, respectively[119]
AlNb$_{1.5}$Ta$_{0.5}$Ti$_{1.5}$Zr$_{0.5}$	*bcc*	Arc Melting	HIPed at 1,400°C and 207 MPa for 2 hours, and then annealed at 1,400°C for 24 hours	A new strategy for developing low-density high-performance RHEAs: 6.9 g/cm^3 to 9.1 g/cm^3,
Al$_{0.4}$Hf$_{0.6}$NbTaTiZr	*bcc*	Arc Melting	HIPed at 1,200°C and 207 MPa for 2 hours, and then annealed at 1,200°C for 24 hours.	Ta and Hf with "low-density" refractory elements (Nb, V, and Zr) and with Ti and Al [120]
Al$_{0.3}$NbTa$_{0.8}$Ti$_{1.4}$V$_{0.2}$Zr$_{1.3}$	*bcc*	Arc Melting		
Ni$_{38}$Cr$_{21}$Fe$_{20}$Ru$_{13}$Mo$_6$W$_2$	*fcc*	Arc Melting	Homogenized at 1,250°C for 120 hours	ICME approach for designing this HEA; exceedingly high corrosion resistance [121]
Mo$_5$Nb$_{10}$Ta$_{35}$V$_{15}$W$_{35}$	*bcc*		Homogenized at 1,000°C in an argon-filled, vacuum-sealed quartz tube for	ICME approach to explore equiatomic and non-equiatomic single phase BCC RHEAs: RHEAs exhibit microhardness and
Mo$_5$Nb$_{25}$Ta$_{30}$V$_5$W$_{35}$	*bcc*	Arc Melting		
Mo$_5$Nb$_{30}$Ta$_{35}$V$_{15}$W$_{15}$	*bcc*			

Composition	Phases	Primary Processing Method	Post Processing Method	Comments
$Mo_5Nb_{35}Ta_{15}V_{10}W_{35}$	*bcc*		24 hours and water quenched	elastic modulus comparable to that of existing RHEAs [122]
$Mo_{10}Nb_{35}Ta_{25}V_5W_{25}$	*bcc*			
$Mo_{15}Nb_{35}Ta_{35}V_5W_{10}$	*bcc*			
$Cr_{20}Mo_{20}Re_{20}V_{20}W_{20}$	*bcc*			
$Cr_5Mo_5Re_{20}V_{35}W_{35}$	*bcc*			
$Ti_2ZrHfV_{0.5}Mo_{0.2}$	*bcc*	Arc Melting	None	Excellent irradiation resistance; no irradiation hardening and abnormal lattice constant reduction after helium-ion irradiation [123]
$Re_{0.56}Nb_{0.11}Ti_{0.11}Zr_{0.11}Hf_{0.11}$	*hcp*	Arc Melting	None [124]	Super conducting HEAs
$(Ti_{20}Zr_{20}Hf_{23})Nb_{21}Re_{16}$	*bcc*	Arc Melting	None [125]	
MoReRhRu	*hcp*		None [126]	
$(MoReRhRu)_{0.9}Ti_{0.1}$	*hcp*	Arc Melting		

3.4.2 Dual Phase HEAs

A total of 35 dual phase HEAs were reviewed, and the summary is presented in Table 3. Out of the 35 HEAs listed below, 26 were manufactured via Arc Melting, 2 were manufactured via Laser Additive Manufacturing Methods, 4 via Vacuum Induction Melting and 3 via other processes.

Table 3: Literature review on various dual-phase HEAs

Composition	Phases	Primary Processing Method	Post Processing Method	Comments
$Al_{15}(CuFeMn)_{85}$	*fcc+bcc*	Vacuum Induction Melting	Homogenization 800°C for 6 hours followed by cold rolling and annealing at 800°C for 1 hour	A new strategy for designing immiscible medium-entropy alloys with excellent tensile properties [127]
$Al_{15}Co_{35}Cu_{35}Mn_{15}$	*fcc+B2*	Vacuum Induction Melting	Homogenization 800°C for 12 hours	Aluminum, a strong B2 former and Mn—a solid solution strengthener is added to immiscible Co-Cu alloy [128]

CoCrFeNiCuAl	fcc+bcc	Arc Melting	None	Compressive YS of 1.82 GPa and plasticity of 20.7% [129]
Al$_{0.3}$CrFe$_{1.5}$MnNi$_{0.5}$	B2+bcc	Arc Melting	Homogenized at 1100°C for 4 h	This alloy at 700°C hardens via TRIP, BCC to tetragonal sigma phase [130]
AlCoCrNi	bcc + B2	Arc Melting	None	AlCoCrNi HEA presented superior strength at high temperatures up to 873 K, which was much higher than that of the commercial Ni-based superalloys. [131]
AlCoCrFeNi	fcc+B2	Arc Melting	None	A series of uniaxial compression tests were performed at target temperatures ranging from 300 to 1173K with a strain rate of 1 × 10−3 s−1. YS at 1,173K was 201MPa with >50% plasticity [40]
AuPdAgPtCuNi	fcc +fcc	Arc Melting	None	Reasonable strength and ductility under compression [103]
AlCrFeCoNiNb	bcc+hexagonal C14 laves	Arc Melting	Homogenized at 1,273K for 1 hour followed by high pressure torsion at 6 GPa	Ultrahigh hardness of 1030 Hv due to the formation of nanograins with an average size of 10 nm [132]
FeRhIrPdPt	fcc+fcc	Arc Melting	None	Magnetic behavior fundamentals [133]
Al$_{0.5}$CoCrCuFeNi	fcc+fcc	Arc Melting	None	YS ~1250MPa, ductility 7.6% [134]
Fe$_{49.5}$Mn$_{30}$Co$_{10}$Cr$_{10}$C$_{0.5}$	fcc+hcp	Vacuum Induction Melting	None	Lower strength and ductility due to inhomogeneity in microstructure [135]
CrFeCoNiAl$_{0.7}$	fcc + B2	Electromagnetic Induction Melting	None	Excellent RT tensile properties with a high YS of 578 MPa, and UTS of 1015 MPa and a large elongation to fracture of ~12 %.[136]
(AlCoCrFeNi)$_{99.95}$Y$_{0.05}$	bcc+B2	Arc Melting	None	YS ~1336MPa, UTS 2402MPa [137]

$Fe_{50}Mn_{30}Co_{10}Cr_{10}$	*fcc+hcp*	Arc Melting	None	Corrosion behavior in H_2SO_4 exhibited lower corrosion resistance and passive film stability than did the CoCrFeMnNi single phase HEA [138,139]
MoNbTaTiZr	*bcc+bcc*	Arc Melting	Stationary Friction Processing (SFP)	SFP to reduce heterogeneity; SFP alloy showed nearly a six times lower corrosion rate in simulated body fluid than as cast [140]
CoCrCuFeNi/Al layers	*fcc+bcc*	Magnetron sputtering	Annealed at 550°C for 1 hour	Remarkably high hardness of 10.4GPa in nano indentation [141]
$Fe_{1.125}Ni_{1.06}CrAl$ $Fe_{1.125}Ni_{1.125}CrAl$ FeNiCrAl	*bcc+bcc*	Arc Melting	None	$Fe_{1.125}Ni_{1.06}CrAl$ I_{corr} of 9.262×10^{-9} A/cm^2 and E_{corr} of − 0.228 V, implying that promising corrosion for industrial applications [142]
FeCrCuTiV	*fcc+bcc*	Arc Melting and DED	None	Grain size and Cu-rich (FCC) phase volume fraction of HEA prepared by DED is smaller and hence has better corrosion resistance [143]
AlFeCoNiCu	*fcc+bcc*	Arc Melting	Homogenized at 1273K for 1 hour and followed by high-pressure torsion at 6 GPa	The capability of the material to store the lattice defects enhances the hardness to 495 Hv and provides an explanation for the reported high compressive strength and good plasticity of this material [144]
CoCrFeNiAlxMn(1−x) x = 0.2 to 0.8	*fcc+bcc*	Laser Cladding	None	Best corrosion resistance with maximum impedance (25,016.228 Ω/cm^2) and the minimum corrosion rate (0.0464 g/m^{2}h) when x = 0.8 [145]
$AlCoCrFeNi_{2.1}$	*fcc+bcc*	Arc Melting	None	$AlCoCrFeNi_{2.1}$ EHEA showed superior molten salt corrosion

				resistance than DS2205 stainless steel (SS), including higher Ni content in EHEA and sacrificial role of Al in reducing outward diffusion of Cr, Fe, and Ni in AlCoCrFeNi$_{2.1}$ and the different reactivity of formation of chlorides, as well as enrichment of Co and Ni in the corrosion layer [146]
Fe$_{47}$Mn$_{30}$Co$_{10}$Cr$_{10}$B$_3$	*fcc+hcp*	Arc Melting	Homogenized at 1 000°C for 12 hour followed by cold rolling and annealing at 1,000°C for 1 – 5 minutes	Fundamental work: Firstly, boride enhances the load-bearing capacity of individual interfaces through an increase in grain boundaries (GB) cohesion, thereby reducing the probability of occurrence of catastrophic interface failure. Secondly, the interface solute decoration and the reduced GB energy introduce an enhanced GB drag effect and a reduced Gibbs-Thomson force during recrystallization, leading to grain-refinement [147]
Al$_{0.5}$CoCrFeNiSi$_{0.25}$	*fcc+bcc*	Vacuum Induction Melting	None	Tensile strength of 1267.8 MPa; fracture toughness of 34.4% [148]
Fe$_{42}$Mn$_{28}$Co$_{10}$Cr$_{15}$Si$_5$	*fcc+hcp*	Vacuum Induction Melting	None	Exceptional superplastic elongation at relatively higher strain rates[149]
AlCrCuFeNi$_x$ (x = 2.0, 2.5, 2.75, 3.0)	*fcc+bcc*	Selective Laser Melting (self-developed LSNF-1 SLM)	None	Deformation nano-twins, stacking faults and strain-activated B2-to-FCC phase transition are discovered in BCC phase [150]
NiAlCoFeNb		Arc Melting	None	Ultra-high hardness of 818Hv for

Composition	Phases	Primary Processing Method	Post Processing Method	Comments
Ni$_{30}$Al$_{30}$Co$_{20}$Fe$_{15}$Nb$_5$	*B2+hexagonal laves phase*			NiAlCoFeNb: Laves phase reinforced alloys generally exhibit high thermal stability and excellent high-temperature mechanical properties [151]
Ni$_{25}$Al$_{25}$Co$_{20}$Fe$_{20}$Nb$_{10}$				
Fe$_{36}$Mn$_{21}$Cr$_{18}$Ni$_{15}$Al$_{10}$	*bcc/B2+fcc*	Arc Melting	None	YS of 750 MPa and 990 MPa in compression and tension respectively at RT. At 600°C tensile and compression YS of the alloy is 310 MPa and 360 MPa, respectively [152]
(AlCoCrFeNi)$_{100-x}$Sc$_x$ HEAs (*x* = 0, 0.5, 1 and 2, at.%)	*B2+bcc*	Arc Melting	None	With an increase of Sc, the YS exhibits an improvement from ~1293 to ~1441 MPa [153]
AlMo$_{0.5}$NbTa$_{0.5}$TiZr	*bcc+bcc*	Arc Melting	HIPed at 1,400°C and 207 MPa for 2 h, and then annealed at 1400°C for 24 h	Two bcc phases were intertwined resulting in a basketweave microstructure: AlMo$_{0.5}$NbTa$_{0.5}$TiZr shows a YS of ~745 MPa with > 50% plasticity in compression at 1,000°C [154]
Al$_{0.3}$NbTaTi$_{1.4}$Zr$_{1.3}$			HIPed at 1,200°C and 207 MPa for 2 hours, and then annealed at 1200°C for 24 hours	
Al$_{0.5}$NbTa$_{0.8}$Ti$_{1.5}$V$_{0.2}$Zr				

3.4.3   Composite HEAs (Precipitate/Dispersion Strengthened)

A total of 33 Composite HEAs were reviewed, and the summary is presented in Table 4. Out of the 33 HEAs listed below, 16 were manufactured via Arc Melting, 10 were manufactured via Laser Additive Manufacturing Methods, 3 via Vacuum Induction Melting and 4 via other processes.

Table 4: Literature review on various composite HEAs

Composition	Phases	Primary Processing Method	Post Processing Method	Comments

$Al_{0.3}Ti_{0.2}Co_{0.7}CrFeNi_{1.7}$	fcc+L1₂	Arc Melting	Solution treated at 1,200°C for 1 hour followed by cold rolling (to 80% reduction) and annealing at 600°C for 50 hours	Low-cost alloy with an extremely high specific strength of 218 MPa/g/cc, as compared to specific strengths of Ni-based alloys (< 150 MPa/g/cm3) and most steels (< 200 MPa/g/ cm³) [155]
$Al_{0.3}Ti_{0.2}Co_{0.7}CrFeNi_{1.7}$	fcc+L1₂	Directed Energy Deposition	None	Mechanical properties identical to conventional counterpart, AD microstructure contained residual stresses [28]
$Al_{10}Nb_{15}Ta_5Ti_{30}Zr_{40}$	B2+bcc	Selective Laser Melting (PROX200 (California, U.S))	None	Low density, high YS: The compressive YS at RT was found to be ~1400 MPa with a plasticity greater than 45% (did not fail) [156]
$Al_{0.3}CoCrFeNi$	fcc +L1₂	Directed Energy Deposition	Annealed at 620°C for 5 hours	Significantly high YS of 600MPa with 20% ductility at RT [24]
$Al_{0.3}CoCrFeNi$	fcc+L1₂	Arc Melting	Homogenization at 1150°C followed by annealing at 620°C for 50 hours	Significantly high YS of 650 MPa with 45% ductility at RT [38]
$Al_{0.2}Co_{1.5}CrFeNi_{1.5}Ti_{0.3}$	fcc+L1₂	Arc Melting	Homogenized at 1,200°C for 48 hours, followed by hot rolling, solution annealing at 1,150°C for 3 hours, and low-temp annealing at 700°C, 800°C, 900°C, and 1,000°C for 1 hour	The optimized mechanical properties, YS of 745 MPa, UTS of 1160 MPa, and elongation to fracture of ~42%, are realized in the HEA aged at 700°C or 800°C for 1 hour [157]
$Al_{0.3}CoCrFeNi$	fcc+B2 +sigma	Arc Melting	Homogenization at 1,150°C followed by cold rolling and annealing at 620°C for 50 hours	Direct annealing for reducing the energy barriers for B2 precipitation [38]

Alloy	Phases	Processing	Heat Treatment	Remarks
Al$_{0.3}$CoCrFeNi	*fcc+B2+* *bcc+sigma*	Arc Melting	Homogenization at 1,150°C followed by cold rolling and annealing at 550°C for 24 hours	Direct annealing for reducing the energy barriers for B2 precipitation [38]
AlCoCrFeNb$_{0.25}$Ni	*bcc +* *(Laves+bcc)*			
AlCoCrFeNb$_{0.5}$Ni	*bcc +* *(Laves+bcc)*	Arc Melting	None	AlCoCrFeNb$_{0.5}$Ni exhibited the highest YS of ~2500MPa and 4.1% plasticity under compression [158]
AlCoCrFeNb$_{0.75}$Ni	*Laves +* *(Laves+bcc)*			
Al$_{0.5}$Co$_{1.5}$CrFeNi$_{1.5}$	*fcc+B2*	Arc Melting	Homogenized at a temperature of 1,150°C for 6 hours followed by cold rolling and annealing at 750°C for 50 hours	The heterogeneous microstructure containing multiple length scales of B2 ppts. Results in a 400% increase in yield stress when compared to the single-phase FCC condition [159]
Al$_{0.5}$Co$_{1.5}$CrFeNi$_{1.5}$	*fcc+L1$_2$*		Homogenized at a temperature of 1,150°C for 6 hours followed by annealing at 750°C for 50 hours	
Al$_{0.3}$CoCrFeNi	*fcc+B2*	Vacuum Induction Melting	Homogenization at 1,150°C for 1 hour followed by cold-rolling and annealing at 800°C for 50 hours	Excellent strength-ductility combination by embedding hierarchical B2 precipitates into a heterogeneous grain structure: YS ~702 MPa and 30% ductility under tension [160]
(Ni$_2$Co$_2$FeCr)$_{92}$Al$_4$Nb$_4$	*fcc+L1$_2$*	Arc Melting	Homogenization was conducted at 1,200°C for 2 hours followed by cold rolling into thin sheets with a total thickness reduction of	This alloy exhibits the highest tensile strength, with UTS of ~1232 MPa and yield stress (YS) of ~ At 600°C, the YS and UTS of this alloy were measured to be ~681

Composition	Phases	Method	Processing	Properties
			~66%. The cold-rolled sheets were subsequently recrystallized at 1,200°C for 1.5 minutes followed by oil quenching and finally aged at 800°C with different durations	MPa and ~991 MPa, respectively. YS anomalies at 760°C with a YS of ~720 MPa and a UTS as high as ~900 MPa, 850 MPa at RT [161].
$Al_{0.3}Cu_{0.5}CrFeNi_2$ + 0.073 at. %C	$fcc+L1_2$ $+M_{23}C_6$	Vacuum Induction Melting	Cold rolled then annealed at 1,000°C for 3 hours and subsequently at 1,200°C for 0.5 hour. Three sets of samples were isothermally aged at 550°C for 150 hours (A550), 700°C for 50 hours (A700), and 900°C for 20 hours (A900), respectively	The synergistic strengthening effects of $L1_2$ phase and $M_{23}C_6$ carbides in the aged samples rendered the improved strength accompanied by the maintenance of a high elongation at RT [162]
FeCoCrNiMn +1.3 at. %C	$fcc+M_{23}C_6$	Arc Melting with electromagnetic stirring	Homogenized at 1,220°C for 6 hours, then the cold rolled followed by annealed for 1 hour at temperatures ranging from 700°C to 1000°C	~1040 MPa with total elongation of ~12% has been achieved in the HEA after annealing at 700°C [163]
$Cr_{19.68}Mn_{19.68}Fe_{19.68}Co_{19.68}Ni_{19.68}Nb_{0.8}C_{0.8}$	$fcc+NbC$	Arc Melting	Homogenized first at 1,473 K for 24 hours and then at 1523 K for another 2 hours	The yield and UTS of the micro alloyed HEA are increased significantly to 732 and 911 MPa, respectively, while retaining a high elongation of 32% [164]
$FeCoCrNiMnTi_{0.3}C_{0.3}$	$fcc+TiC+M_{23}C_6+M_7C_3$	Mechanical alloying followed by Vacuum Hot pressing	None	Compression YS~ 1445 MPa, plastic strain 11.5% and compression strength 1999 MPa [165]

Alloy	Phase	Synthesis	Heat Treatment	Properties
$CoCrFeNiMnC_{0.2}$	*fcc+M_7C_3*	Arc Melting	None	YS ~700MPa, plasticity 10% [166]
$(Fe_{40}Mn_{40}Co_{10}Cr_{10})_{3.2}C_{6.8}$	*fcc+$M_{23}C_6$*	Arc Melting	None	YS~620MPa 26.5% ductility [167]
CoCrFeMnNi +1.84 at. % C	*fcc+$M_{23}C_6$ +M_7C_3*	Arc Melting	Homogenized for 24 hours at 1,050°C followed by cold rolling and annealing at 900°C for 1 hour	YS~527MPa ductility 40% [168]
$Fe_{19.84}Mn_{19.84}Ni_{19.84}Co_{19.84}Cr_{19.84}C_{0.8}$	*fcc+$M_{23}C_6$*	Vacuum Induction Melting	Hot-rolled at 950°C followed by homogenization at 1,200°C for 3 hours followed by cold-rolling and annealing at 900°C in Ar for 3 minutes	YS of ~1030 MPa and UTS of ~1170 MPa with uniform elongation of ~11% [169]
FeCoCrNiMn + 1.0 at. %C	*fcc+$M_{23}C_6$*	Arc Melting	Homogenization annealed at 1,100°C for 12 hours followed by cold rolling and annealing at 800°C for 1 hour	YS~638MPa Ductility 30% [170]
$Fe_{40.4}Ni_{11.3}Mn_{34.8}Al_7.5Cr_6$ + 1.1 at. %C	*fcc+B2+M_7C_3 +$M_{23}C_6$*	Arc melting	Cold rolled and annealed at 1073K for 8 hours; 1173K for 8 hours; 1273K for 1 hour; 1273K for 8 hours; and 1373K for 4 hours	YS ~557MPa ductility of 25% [171]
$CoCrFeNiV_{0.5}C_x$ *(x = 0.01, 0.02, 0.03 and 0.04)*	*fcc+M_7C_3*	Arc Melting	Hot rolled to a 20% reduction in thickness, followed by homogenized at 1,200°C for 3 hours, followed by water cooling treatment. After that, rolling amount of cold rolling was 70%, followed by annealing 600°C	The YSs(σ_y) of $CoCrFeNiV_{0.5}C_{0.02}$ and $CoCrFeNiV_{0.5}C_{0.03}$ alloys annealed at 700°C are 1339.7 MPa and 1264.6 MPa, respectively, with excellent performance [172]

			for 1 hour, 700°C for 1 hour, and 800°C for 1 hour.	
CoCrFeMnNi + 5 wt. %NbC	*fcc+Nb segregation at dislocation cell boundaries*	Selective Laser Melting	Few specimens are annealed at 800°C for 2 hours	YS ~870 MPa at RT and 420MPa~at 800°C: The dislocation cells in this-HEA are stable and a superior combination of thermal stability and strength is achieved through the addition of NbC nanoparticles [173]
CoCrFeMnNi + 5 wt.% TiB2	*fcc+TiB$_2$*	Directed Energy Deposition	None	The TiB$_2$ acts as nucleation sites and promotes the formation of grain-refined and dislocation-populated microstructures. YS of ~600MPa at RT. Self-lubricating wear resistance [174]
Co$_{1.5}$CrFeNi$_{1.5}$Ti$_{0.5}$Mo$_{0.1}$	*fcc+L1$_2$*	Selective Laser Melting (EOSINT M280, EOS Corporation) and Electron Beam Melting (Arcam A2X; Arcam AB)	Solution treated at 1393K for 3 hours	The solution-treated SLM (1400MPa) and EBM (1300MPa) specimens exhibited higher tensile strength than those of conventional high-corrosion-resistant alloys in harsh, corrosive environments, such as duplex stainless steels (Duplex stainless steel: 655 MPa Super duplex stainless steel: 750–800 MPa and Ni-based super alloys (Alloy C276: 690 MPa, Alloy 718: 1275 MPa)[175]
TiZrHfNb$_{0.6}$	*bcc + omega*	Directed Energy Deposition	None	Poor mechanical properties; embrittlement due to omega precipitation [176]

Composition	Phases	Processing Method	Post Processing	Comments
CrMnFeCoNi + 1.5 at.%C (C-HEA)	fcc+$Cr_{23}C_6$	Selective Laser Melting (Concept Laser Mlab Cusing)	Annealed at 650°C for 1 hour	Microstructural evolution did not occur, even in crept sample at a creep strain of 7% under applied stress of 325 MPa at 500°C [177]
GRX 810 (Developed by NASA) (Co-33%, Cr-29%, Re-1.5%, Al-0.3%, Ti-0.25%, Nb-0.75%, W-3%, C-0.05%, Ni-Balance) all in wt.%	fcc+$carbides$+Y_2O_3	Selective Laser Melting (EOS M280)	None	The best material for creep, oxidation, and strength at higher temperatures [178]
NiCoCr + 1 wt% Y_2O_3	fcc+Y_2O_3	Selective Laser Melting (EOS M280)	None	This new processing technique employed resonant acoustic mixing to coat an equiatomic NiCoCr powder with nano-scale yttrium oxides [179]

3.5 Meta Stable HEAs

3.5.1 TRIP/TWIP HEAs

A total of 21 Meta Stable HEAs were reviewed, and the summary is presented in Table 5. Out of the 21 HEAs listed below, 16 were manufactured via Arc Melting and 5 via Vacuum Induction Melting.

Table 5: Literature review on various meta stable HEAs

Composition	Phases	Primary Processing Method	Post Processing Method	Comments
49.5Fe-30Mn-10Co-10Cr-0.5C (at. %)	fcc	Arc Melting	Hot rolling followed by homogenization at 1,200°C for 2 hours, then cold rolled and annealed at 400, 650 and 750°C	Nano twin/nano grained engineered fcc microstructure exhibited 1.3GPa; the fcc grains transformed to hcp martensite [180]
$Co_{35}Cr_{20}Mn_{15}Ni_{15}Fe_{15}$			Homogenized at 1473 K for 5 hours subsequently forged at 1473 K to a 50% reduction in thickness. The forged samples were	TWIP; YS 231 MPa, UTS 688 MPa [181]
$Co_{35}Cr_{25}Mn_{15}Ni_{15}Fe_{10}$	fcc	Arc Melting		TRIP; YS 305 MPa, UTS 806 MPa [181]

Composition	Phase	Synthesis	Processing	Properties
			aged at 1273 K for 10 minutes by RT rolling to a 40% reduction in thickness. Finally, the samples were aged at 1273K for 6 minutes.	
$Fe_{40}Mn_{10}Co_{20}Cr_{20}Ni_{10}$	*fcc*	Vacuum Induction Melting	Hot-rolled at 900°C followed by homogenization at 1200°C for 2 hours. After homogenization, the HEA was cold-rolled subsequently annealed at 800°C for 30 minutes, followed by water-quenching.	YS~ 375 MPa UTS ~785 MPa Ductility: 77.5% fcc → hcp [182]
$Cr_{20}Mn_{24}Fe_{30}Co_{20}Ni_6$	*fcc+sigma*	Vacuum Induction Melting	Hot-rolled at 900°C followed by homogenization at 1250°C for 2 hours. After homogenization, the HEA was cold-rolled subsequently annealed at 800°C for 5 – 10 minutes followed by water-quenching.	TRIP: high strength but low ductility [183]
$Cr_{20}Mn_{15}Fe_{34}Co_{20}Ni_{11}$	*fcc*			TWIP: better combination of strength and ductility [183]
$Fe_{50}Mn_{25}Ni_{10}Cr_{15}$	*fcc*	Arc Melting with Electromagnetic Stirring	Cold rolled followed by homogenization at 1173K for 10 minutes	Tensile strength of ~ 0.98 GPa and ductility of ~83 % at 77 K, TRIP and TWIP [184]
$(NiCoCr)_{92}Al_6Ta_2$	*fcc*	Arc Melting	Homogenization treatment at 1,225°C for 24 hours followed by cold rolling to a sheet with a thickness reduction of 70%. Finally, the cold-rolled sheets were rapidly heated to 1,150°C within ~20 seconds and dwelled for 3 minutes	Testing temperature from 298 down to 77 K, the YS, ultimate strength, and tensile ductility are increased from ~600 to ~800 MPa, from ~1.0 to ~1.35 GPa and from ~52% to ~90% [185]
$Fe_{50}Mn_{30}Co_{10}Cr_{10}$	*fcc+hcp*	Vacuum Induction Melting	Hot-rolled at 900°C followed by homogenization at 1,200°C for 2 hours.	FCC γ to HCP ε, formation of stacking faults & dislocation slip in the FCC γ phase. At later

			For various grain sizes and phase fractions, the homogenized alloy was cold-rolled and subsequently annealed at a furnace temperature of 900°C in Ar for 3 – 60 minutes.	stages of deformation, additional mechanical twinning, dislocation slip, and formation of stacking faults in HCP ε phase are also activated as important deformation mechanisms. This shows that the HCP ε phase also partitions a certain portion of the imposed load. YS 305MPa and UTS 830 MPa [186]
$Cr_{20}Mn_6Fe_{34}Co_{34}Ni_6$	*fcc + hcp*	Vacuum Induction Melting	Hot-rolled at 900°C followed by homogenization at 1,200°C for 3 hours; the homogenized alloy was cold-rolled and subsequently annealed at a furnace temperature of 800°C for 1 hour.	YS 600MPa and UTS 1000MPa [187]
$Ti_{60}Mo_{10}V_{10}Cr_{10}Zr_{10}$	*bcc*	Arc Melting	None	Compressive YS ~1298 MPa UTS~2000MPa; plasticity 33.4% [189]
$Ti_{35}Zr_{27.5}Hf_{27.5}Nb_5Ta_5$	*bcc*	Arc Melting	The control of structure and the grain size was carried out by cold rolling with a 60% and 70% reduction in thickness followed by a 30-minute solution treatment under helium at 900°C and 800°C, respectively	YS~ 540 MPa and UTS ~995 MPa, ductility ~23% Bcc → orthorhombic [190]
$Ti_{55-x}Zr_{20}Hf_{15}Al_{10}Nb_x$ (*x*=5-8, at%)	*bcc*	Arc Melting	None	YS~ 735 MPa and UTS ~1051 MPa, bcc → orthorhombic [191]
$Ti_{35}Zr_{27.5}Hf_{27.5}Nb_5Ta_5$	*bcc*	Arc Melting	None	YS ~121 MPa, UTS, 574 MPa

$Ti_{38}Zr_{25}Hf_{25}Ta_{10}Sn_2$				YS ~407 MPa, UTS, 925 MPa
$Ti_{38}Zr_{25}Hf_{25}Ta_7Sn_5$				YS ~232 MPa, UTS, 409 MPa bcc →hcp [192]
$Ti_{40}Zr_{25}Nb_{25}Ta_{10}$				YS ~910MPa, UTS, 1040 MPa
$Ti_{45}Zr_{25}Nb_{25}Ta_5$	*bcc*	Arc Melting	None	High corrosion resistance and good biocompatibility [192]
$Ti_{48}Zr_{20}Hf_{15}Al_{10}Nb_7$	*bcc*	Arc Melting	Cold-rolled into sheets with 30% reduction in thickness and then annealed at 800°C and 900°C for 30 minutes	~900 MPa UTS YS~700 MPa Bcc → orthorhombic [193]
Fe-20Mn-20Co-15Cr-5Si-1.5Cu	*fcc*	Vacuum Induction Melting	Homogenized (1,100°C) in the γ-fcc region for 2 hours to obtain maximum γ-fcc and then rolled at 900°C (γ-fcc domain) to a final thickness of ~6.5 mm, to get rid of the casting defects. The rolled sheet was then descaled and heated to 500°C and then warm-rolled to a final thickness of ~3.15 mm.	σ-bct phase in the higher combination of dpa and temperature, the extreme case of 100 dpa/500°C. Resistant to void formation and swelling. Reversing the irradiation-induced transformation by temperature-induced transformation and thus minimizing degradation due to irradiation [194]

3.6 Survey on Prior HEA research for nuclear applications

This section discusses the HEAs that were specifically developed targeting nuclear applications. A total of 40 HEAs were reviewed, and the summary is presented in Table 6. Out of the 40 HEAs listed below, 20 were composite HEAs, 19 were single phase HEAs and 1 was a dual phase HEA. Since, the literature survey identifies the potential in both single and composite HEAs, we have down selected HEAs in both the categories for further investigation, and the experimental results are presented in Section 4 of the report.

Composition	Phases	Primary Processing Method	Post Processing Method	Comments
$V_{35}Ti_{35}Fe_{15}Cr_{10}Zr_5$ Classification: Dual Phase HEAs	*bcc+bcc* Dendritic microstructure	Vacuum Arc Melting	Annealed at 1,000°C for 3 hours for comparison	Compression YS ~ 224MPa @900°C. ~346 MPa @800°C Design: Fe, Cr, Ti, V, and Zr low activation elements for fusion and Zr for solid solution strengthening No irradiation was performed [195]
$W_xTaTiVCr$ (x=0.3 -0.9) Classification: Composite HEAs	*bcc+TiC+C15 laves*	SPS	None	X=0.32-0.63; The compressive strength (~2000 MPa) is two-fold higher than those of pure W and W-containing HEAs Low activation elements [196]
TiVNbTa Classification: Single Phase HEAs	*bcc*	Vacuum Arc Melting	None	Low activation elements The difference in the hardness values before and after irradiation is negligible <5% No radiation induced hardening [197]
TiVZrTa Classification: Composite HEAs	*bcc+bcc+bcc*	Vacuum Arc Melting	none	Low activation elements The difference in the hardness values before and after irradiation is negligible <5% No radiation induced hardening [197]
TiVCrTa Classification: Composite HEAs	*bcc+Laves*			
NiCoCr Classification: Single Phase HEAs	*fcc*			NiCoCr show significantly less defect clustering compared to Ni and NiFe alloys [198]

Al$_{0.1}$CoCrFeNi Classification: Single Phase HEAs	*fcc*	VLM	none	The volume swelling of fcc is the least among the three. 1.25% @ 50 dpa at RT. The volume swelling in AlxCoCrFeNi alloys in the ascending order is: FCC< FCC + BCC<BCC, while the order is BCC< FCC for conventional nuclear materials. The irradiation-induced volume swellings in AlxCoCrFeNi HEAs are significantly lower than conventional nuclear materials under similar irradiation dosages [199]
Zr$_{32}$Hf$_{30}$Nb$_{38}$ Classification: Single Phase HEAs	*bcc* (Nano crystalline)	Sputter Deposition (1 mm thick)	None	High intensity electron beam of 2 MeV: The structure remained unchanged up to 12 dpa at 298K (25°C) and up to 40 dpa at 103K (−170°C) Atomic level strains are principal mechanism for radiation resistance [200]
HfTaTiVZr Classification: Single Phase HEAs	*bcc*	Arc Melting	none	There is no change in hardness value up to 750°C Increase in hardness and YS for the HEA was ~20% and for SS304 was ~50% under identical irradiation conditions. Better irradiation resistance of the HEA was attributed to its self-healing ability. Sluggish diffusion of atoms in the HEA reduced effective interstitial and vacancy mobility and limited

Alloy / Classification	Phase	Processing	Heat Treatment	Notes
				irradiation induced damage [201]
$W_{38}Ta_{36}Cr_{15}V_{11}$ Classification: Single Phase HEAs	*bcc* bimodal grain size distribution with ~70% of the grains with sizes in the nanocrystalline regime (≤100 nm) and some regions of ultrafine grain sizes (100 to 500 nm)	Magnetron sputtering deposition	None	Concurrent transmission electron microscopy (TEM) and APT analyses demonstrate the existence of a second phase rich in Cr and V, first forming lamella-like regions to transform to quasi-spherical precipitates after irradiation. Irradiation at 800°C at 8dpa did not reveal any dislocation loops but precipitation at nano scale occurred. A slight hardening is also observed [202]
CoCrFeMnNi-5wt.%NbC Classification: Composite HEAs	*fcc+Nb segregation at dislocation cell boundaries*	Selective Laser Melting	Few specimens are annealed at 800°C for 2 hours	YS ~870 MPa at RT and 420MPa~at 800°C: The dislocation cells in this-HEA are stable and a superior combination of thermal stability and strength is achieved through the addition of NbC nanoparticles [203]
$(Ni_2Co_2FeCr)_{92}Al_4Nb_4$ Classification: Composite HEAs	*Fcc+L1_2*	Arc Melting	Homogenization was conducted at 1,200°C for 2 hours followed by cold rolling into thin sheets with a total thickness reduction of ~66%. The cold-rolled sheets were subsequently recrystallized at 1,200°C for 1.5 minutes, followed by oil quenching and finally aged at	This alloy exhibits the highest tensile strength, with UTS of ~1232 MPa and yield stress (YS) of ~ At 600°C, the YS and UTS of this alloy were measured to be ~681 MPa and ~991 MPa, respectively. YS anomalies at 760°C with a YS of ~720 MPa and a UTS as high as ~900 MPa,850 MPa at RT [161]

Alloy / Classification	Phase	Processing	Heat Treatment	Notes
			800°C for 24 hours	
NbTiVZr$_{0.5}$ Classification: Composite HEAs				Whilst the neutron cross-sections of the alloys are markedly higher than Zr, the combination of properties required for future advanced nuclear reactors operating at increased temperatures may be advantageous.
NbTiVZr Classification: Composite HEAs	*bcc+hcp*	Arc Melting	Homogenized at 1,200 ± 10 °C (1473 ± 10 K) for 100 h followed by annealing at 700°C for 100 hours	
NbTiVZr$_2$ Classification: Composite HEAs				Low neutron cross section elements [204]
MoNbCrVTi Classification: Single Phase HEAs	*bcc*	Vacuum Arc Melting	None	Low thermal neutron cross section elements.
MoNbCrZrTi Classification: Composite HEAs	*bcc +Laves*			The MoNbCrVTi alloy exhibits a hardness of 494.4 ± 7.7 *Hv*, a high YS of 1281 MPa, and fractured at a strain of 9.4% at RT [205]
Ti$_2$ZrHfV$_{0.5}$Mo$_{0.2}$ Classification: Single Phase HEAs	*bcc*	Vacuum Arc Melting	None	Ti: good corrosion resistance. Mo and V elements: good high temperature performance Hf and Zr elements: good neutrons-penetrating properties Lattice constant decreases after irradiation; first to report the abnormal X-ray diffraction phenomenon of metallic alloys after irradiation. Almost no hardening after irradiation [206]
MoNbTaW Classification: Single Phase HEAs	*bcc*	Vacuum Arc Melting	Solution treated at 1,200°C /1,500°C	(MoNbTaW: 550 Hv, MoNbTaTi: 420 Hv, MoNbTaTiW: 479 Hv)

Alloy / Classification	Phase	Process	Heat treatment	Remarks
MoNbTaTi Classification: Single Phase HEAs				Irradiation hardening of MoNbTaTiW is less than that of MoNbTaTi, possibly because of the high entropy effect. There is no noticeable irradiation hardening of MoNbTaW.
MoNbTaTiW Classification: Single Phase HEAs				At a depth of 350 nm, the irradiation hardening of MoNbTaTi and MoNbTaTiW was less than that of pure W [207]
$Mo_{0.5}VNbTiCr_x$ (x = 0, 0.25, 0.5, 0.75, 1.0, 1.5 and 2.0) Classification: Composite HEAs	*bcc+fcc+laves*	HIP	None	Cr0, Cr0.25, Cr0.5 and Cr0.75-single-phase BCC Cr1.0, Cr1.5 and Cr2.0- BCC +C15 Laves phase+ FCC (TiC/N) The YS increases from 1135 MPa for the Cr0 alloy to 2311 MPa for the Cr2.0 alloy. Mo0.5VNbTi and Mo0.5VNbTiCr0.25 alloys exhibit superior corrosion resistance than the Zr-4 alloy in superheated steam at 400°C and 10.3 MPa [208]
$Fe_{38}Mn_{40}Ni_{11}Al_4Cr_7$ Classification: Single Phase HEAs	*fcc*	Vacuum levitation melting	Annealed at 530°C for 4 hours	Interstitial carbon can inhibit the irradiation hardening of HEAs. The hardening rate of the C0 sample is 65.56%, whereas those of the C0.2, C0.5 and C1.0 samples are 34.8%, 43.6% and 24.92%, respectively [63]
$Ti_{48.2}V_{44}Cr_{3.6}Al_{4.2}$ Classification: Single Phase HEAs	*bcc*	Vacuum levitation melting	None	YS ~800MPa with 35% ductility at RT [209]

$Al_{20}Be_{20}Fe_{10}Si_{15}Ti_{35}$ Classification: Composite HEAs	*Ordered Hexagonal+minor intermetallics (Ti,Fe)Al$_2$ and Ti$_5$Si$_3$*	Vacuum Arc Melting	None	Density of 3.91 g cm^{-3} and exhibits a high hardness of HV 911 Excellent oxidation resistance at 700°C and 900°C, which is much better than Ti-6Al-4V. Therefore, the present alloy is promising for high-temperature applications requiring lightweight, wear-resistant, and oxidation-resistant components [210]
$W_{29.4}Ta_{42}Cr_{5.0}V_{16.1}Hf_{7.5}$ Classification: Single Phase HEAs	*bcc*	Magnetron-sputtering deposition	None	Showed only approximately 10 nm change in grain size after ~8.45 at. % He implantation Grain refinement observed during dual-beam irradiation Depletion of Hf from grain boundaries during irradiation which can be attributed to the Inverse Kirkendall effect and/or ballistic mixing during irradiation. No loop formation and the total change in volume is ~0.3 % after 8.45 dpa and higher percentage of implanted He [211]
$Zr_{35}Ti_{30}Nb_{20}Al_{10}Ta_5$ Classification: Composite HEAs $Zr_{35}Ti_{30}Nb_{20}Al_{10}V_5$	*bcc+B2*	Vacuum Arc Melting	None	Low neutron absorption cross sections Tensile YS of ~850 MPa/~848 MPa with elongation of ~25%/~16% at RT [212]

Classification: Composite HEAs				
AlCrFeNiTi$_x$ (x = 0, 0.5, 1) Classification: Composite HEAs	bcc+B2	Argon Levitation Melting	None	Size of dislocation loops in the BCC phase was smaller than that in the B2 phase for AlCrFeNi. Small size and large density of dislocation loops formed in Ti0.5 especially in B2 phase. Ti nanoparticles in B2 has caused a high entropy effect that hinders the movement of defects, showing the relatively excellent radiation resistance than compared to BCC [213]
CrNbTaVW Classification: Composite HEAs CrNbTaVW$_{1.7}$ Classification: Composite HEAs	bcc +other minor phases	Upgraded Field Assisted Sintering	None	Effect of irradiation was more severe in CrNbTaVW1.7 when compared to CrNbTaVW, evidencing swelling in all the surface [214].
NiCoCrFePd Classification: Single Phase HEAs	fcc	Vacuum Arc Melting	1,200°C temperature for 24 hours	Resistance against irradiation hardening behavior at high fluence under 1.05 MeV Xe+3 ion irradiation. Simultaneous recrystallization and recombination of point defects lead to the softening effect in the mechanical behavior at higher fluence, which is a good sign of resistance towards mechanical failure [215]
(3.1-Cr, 5.9-Nb, 21.7-Ta, 3.3-Ti, 21.7-W)-44.3 at.%C [HEC]	fcc	Direct Current- Magnetron Sputtering	None	HEC and HEA have not displayed any local chemical instabilities (such as RIS and RIP)

Alloy / Classification	Crystal Structure	Synthesis		Properties / Notes
Classification: Single Phase HEAs				because of the atomic collisions on their microstructures.
1.8-Cr, 9-Nb, 46-Ta, 1.1Ti, 42.1-W [HEA] Classification: Single Phase HEAs	bcc			Surprisingly, amorphization did not occur for the HEC up to 10 dpa in the temperature of relevance for light-water reactors. HEC having a slightly higher radiation tolerance than the HEA [216]
$CrFeNi_{2.5}Mo$ Classification: Composite HEAs	fcc+fcc+sigma			Co- and Cu-free HEAs $Al_{1.0}CrFeNi_{2.5}$ alloy exhibits excellent mechanical properties with the UTS, elongation, and hardness of 1090 MPa, 16.8% and 336 HV
$Al_{1.0}CrFeNi_{2.5}$ Classification: Composite HEAs	fcc+bcc+bcc	Arc Melting and Copper Mold Suction Casting	None	
$Al_{0.5}CrFeNiMo_{0.5}$ Classification: Composite HEAs	fcc+fcc+bcc+ sigma			The E_{corr}, I_{corr} and I_{pass} results indicate that $Al_{0.5}Mo_{0.5}$ alloy possesses excellent comprehensive corrosion resistance in 3.5 wt.% NaCl with the lowest I_{corr} and I_{pass} as well as a more positive E_{corr} [217]
$Al_{0.2}CrFeNiMo_{0.8}$ Classification: Composite HEAs	fcc+fcc+sigma			
$Al_{0.8}CrFeNiMo_{0.2}$ Classification: Composite HEAs	fcc+bcc+ sigma			
$Nb_{25}Mo_{25}Ta_{25}W_{25}$ Classification: Single Phase HEAs	bcc	Vacuum Arc Melting	None	RT to 1,600°C compression properties RT: 1100 MPa peak strain 2% 800°C: 552MPa and ductility >22% 1000°C: 548 MPa 1,600°C: 405 MPa [218]

3.7 Promising HEA candidates for nuclear applications based on all HEAs surveyed.

Few HEAs that can be recommended based on the literature survey presented in the previous Sections is as follows:

(1) $Al_{0.3}Cu_{0.5}CrFeNi_2$, $Al_5Cr_{12}Fe_{35}Mn_{28}Ni_{20}$ and $Al_{10}Cr_{12}Fe_{35}Mn_{23}Ni_{20}$ are FCC based High Entropy Alloys suggested by the USNRC report titled "Use of High Entropy Alloys (HEAs) in Future Nuclear Applications" published in January 2023. All the three alloys exhibit good mechanical properties at RT.

(2) $(Ni_2Co_2FeCr)_{92}Al_4Nb_4$ is a precipitation strengthened HEA exhibiting ~500MPa Yield Strength with a ductility of ~6% at 870°C. It is one of the few HEAs that exhibit remarkable high temperature mechanical properties.

(3) GRX-810 is a ODS strengthened alloy recently developed by NASA with high temperature (at 1093°C) creep performance 2-3 orders of magnitude better than the current high temperature alloys. Since, GRX-810 is mainly three component NiCoCr based alloy with minor additions of other elements such as Al, Ti, Nb, W, and C and it may not be strictly classified under the category of high entropy alloys. However, this material can be best classified as a medium entropy alloy or an ODS alloy due to the presence of Y_2O_3 particles. ***Therefore, we recommend pursuing this material under a different work package under the AMMT program.***

(4) $Al_{0.3}Ti_{0.2}Co_{0.7}CrFeNi_{1.7}$ is a precipitation strengthened FCC HEA reported to exhibit a yield strength of ~1630 MPa, and good tensile ductility of ~15% at room temperature, which is significantly higher than most Stainless Steels. This HEA is also expected to have high-temperature stability up to ~1100 °C.

4.0 Experimental Work

The primary objective of this work is to conduct advanced manufacturing feasibility studies on the down selected promising HEAs based on the elaborate literature survey presented in Section 3 of this report. This provides information to evaluate the benefits (if any) of advanced manufacturing methods that enable bulk economic manufacturing routes and may additionally further enhance the properties of the selected HEAs. The advanced manufacturing routes include both liquid and solid-state manufacturing approaches. Table 7 below summarizes the experimental work executed to date in fiscal year 2023 (FY23) and the work in progress. ShAPE is considered for the two down-selected HEAs ($Al_{0.3}Ti_{0.2}Co_{0.7}CrFeNi_{1.7}$ and $Al_{10}Cr_{12}Fe_{35}Mn_{23}Ni_{20}$) due to its unique processing conditions which result in finer microstructures with compositionally homogenous grains that would potentially enhance the mechanical properties. In addition, the effect of solid phase processing on the mechanical properties of a single-phase HEA can also provide valuable information and potential more economical routes to HEA adoption to the markets. It is therefore also recommended that a functional graded alloy to HEA as a final coating begin explored to determine the impact on the interlayers and interface properties. Technical detail of the work completed are provided in sections below.

Table 7: Experimental work completed and tasks in progress.

HEA	Tasks completed	Tasks in progress
$Al_{0.3}Ti_{0.2}Co_{0.7}CrFeNi_{1.7}$ Classification: Composite HEA (See Section 4.1)	1. Microstructural characterization on laser powder bed fusion (LPBF) and DED samples (as processed and annealed conditions). 2. Nanoindentation testing from RT to 500°C on LPBF and DED samples (as processed & annealed conditions)	1. ShAPE processing on the cast counterpart followed by complete microstructural characterization 2. Nanoindentation testing at 800°C on LPBF, DED, ShAPE, and cast samples (as processed & annealed conditions)
$Al_{10}Cr_{12}Fe_{35}Mn_{23}Ni_{20}$ Classification: Composite HEA (See Section 4.3)	1. Procured cast rods	1. Heat treatment 2. ShAPE processing on the cast rods followed by complete microstructural characterization of both as-cast and ShAPE processed samples 2. Nanoindentation testing at 800°C on the ShAPE, cast and heat-treated samples
Compositionally Graded HEA SS316 to $CoCrNiFe_{0.5}$ (with trace amounts of Ta, Ti, Mo, Si, and Nb)	1. Samples manufactured by DED 2. Microstructural characterization at the interface between the substrate (SS316)	1. Microstructural characterization on a few other regions of interest in the graded HEA 2. Nanoindentation testing at 500 °C and 800°C on the DED

	and base layer of the graded HEA	fabricated graded HEA (multiple layers including substrate)
Classification: Single Phase HEA ((See Section 4.2)	3. Microstructural characterization at the interface between matrix (HEA) and un-melted powder particle (SS316)	3. ShAPE processing on a graded material and single-phase HEA, followed by high temperature mechanical properties.

4.1 Down selected HEA: $Al_{0.3}Ti_{0.2}Co_{0.7}CrFeNi_{1.7}$

4.1.1 Background

$Al_{0.3}Ti_{0.2}Co_{0.7}CrFeNi_{1.7}$ HEA is a precipitation strengthened alloy reported to exhibit a yield strength of ~1600 MPa with decent ductility at room temperature (RT) and is expected to have high-temperature stability up to ~1100°C [16]. This HEA was fabricated via two different AM techniques: DED and SLM. The evolution of the heterogeneous microstructures in the AD and subsequently annealed conditions and their tensile properties at RT has been reported previously [29,219]. However, the temperature-dependent mechanical behavior essential for nuclear applications was not yet investigated. This report provides a discussion on the microstructural differences as well as the temperature-dependent (from RT to 500°C) nanoindentation behavior of the heterogeneous microstructures obtained via one-step annealing, post DED, and SLM processing of $Al_{0.3}Ti_{0.2}Co_{0.7}CrFeNi_{1.7}$ HEA. The differences in the nanoindentation behavior between the AD and the one-step annealed conditions of the DED and SLM processed conditions are determined. The work presented in Section 4.1 is accepted for publication in a peer reviewed journal [220].

4.1.2 Materials and Methods

This study used the Optomec LENS-750 system equipped with an IPG YLS-1500 fiber laser system (with a maximum power output of 1500 W) for the DED and Trumpf TruPrint 1000 laser powder bed fusion system used for SLM. Pre-alloyed powders of $Al_{0.3}Ti_{0.2}Co_{0.7}CrFeNi_{1.7}$ HEA procured from TOSOH, SMD were used for both DED and SLM processing. The samples were provided by University of North Texas.

The AD specimens from DED (referred to as DED(AD)) and SLM (referred to as SLM(AD)) were sectioned using the KENT USA (WSI-200) electric discharge machine (EDM). Sections from DED(AD) and SLM(AD) conditions were then individually encapsulated in a quartz tube backfilled with argon for the heat treatments (800°C for 5 hours followed by water quenching). These conditions will be hereafter referred to as DED(HT) and SLM(HT).

Scanning electron microscopy (SEM) imaging was performed on all four conditions in an FEI-Quanta Nova-Nano SEM 230. Nanoindentation tests (Hysitron Inc., Minneapolis, MN, USA) were performed at RT, 250°C, and 500°C using a Sapphire Berkovich tip. The tests were carried out at 1000 mN load with a loading time of 5 seconds, holding time of 2 seconds, and unloading time of 5 seconds. 50 μm spacing between indents was used to avoid overlap of plastic zones from adjacent indents. The high temperature indentations were done in $Ar+H_2$ atmosphere to minimize oxidation of the samples and the system was allowed to stabilize at each temperature for at least 15 minutes before performing the indentations. A minimum of 25 good indents were used for hardness calculations for statistics.

The phase fraction versus temperature plot for $Al_{0.3}Ti_{0.2}Co_{0.7}CrFeNi_{1.7}$ HEA was simulated using Thermo-Calc software (with TCHEA3 database).
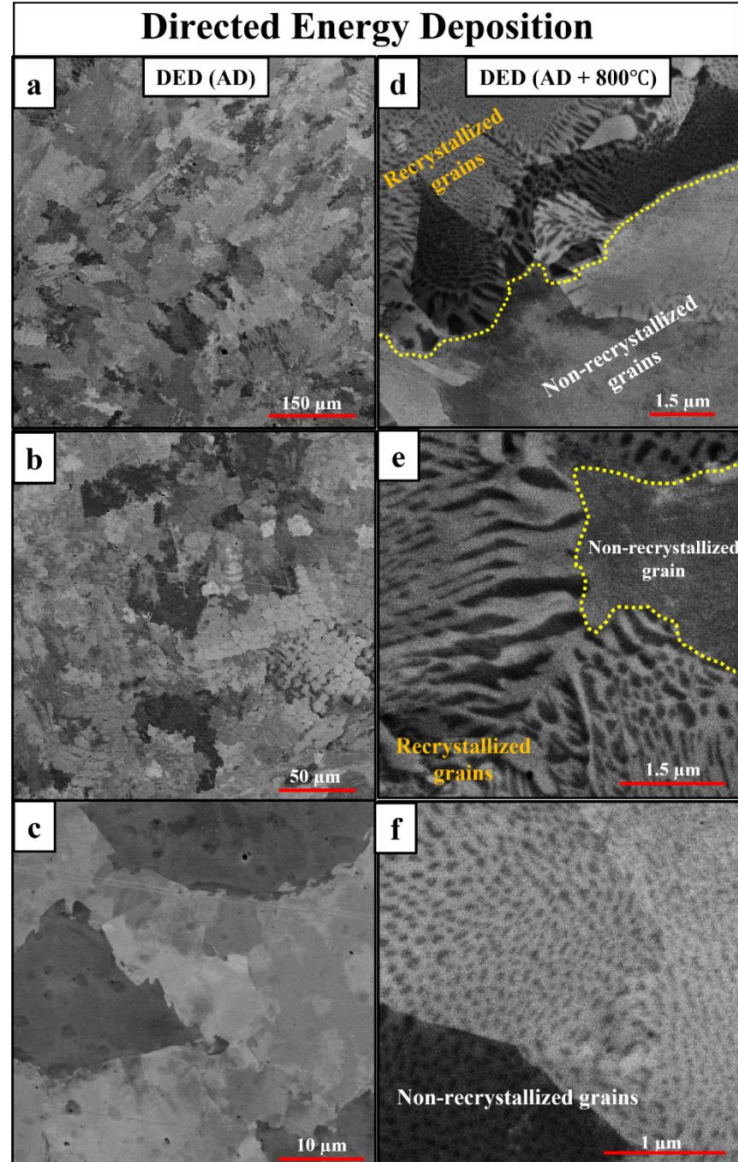
4.1.3   Results and Discussion

Figure 3: Low, medium, and high magnification SEM backscattered images for (a-c) DED (AD) and (d-f) DED (HT or AD+800°C) conditions of DED processed $Al_{0.3}Ti_{0.2}Co_{0.7}CrFeNi_{1.7}$ HEA.

The SEM backscattered images from the as-deposited (DED(AD)) and the one-step annealed conditions (DED(HT)) of the DED processed $Al_{0.3}Ti_{0.2}Co_{0.7}CrFeNi_{1.7}$ HEA are shown in Figure 3 (a-c) and Figure 3(d-f), respectively. The DED as-deposited condition shows a single-phase (FCC) microstructure with reasonably large, peculiar-shaped [23] grains often with jagged grain boundaries. Additionally, some grains also exhibit solidification cells presumably arising from compositional segregation due to the high solidification rates involved in DED processing. However, the possible formation of early-stage nanoscale $L1_2$ precipitates within the FCC matrix

of the DED(AD) condition was previously observed in high-energy synchrotron X-ray diffraction results [219]. The annealing heat treatment (800°C for 5 hours) conducted on the DED-processed HEA led to the partial recrystallization of FCC grains and a significant growth of the non-recrystallized FCC grains. The grain size of the non-recrystallized grains increased from ~81 μm in the DED(AD) to ~159 μm in the DED(HT) condition [219]. The annealing heat treatment also resulted in the formation of $L1_2$ precipitates with two different morphologies within the FCC matrix. The SEM images in Figure 3(d-e) reveal the rod-like $L1_2$ precipitates in the recrystallized FCC grains, while the SEM image in Figure 3 (f) shows the *equiaxed/*near-spherical $L1_2$ precipitates in the non-recrystallized grains. The precipitation mechanism fundamentally differs between the two kinds of grains: continuous precipitation in the non-recrystallized grains and discontinuous precipitation in the recrystallized grains, leading to different morphologies for the $L1_2$ precipitates [219].
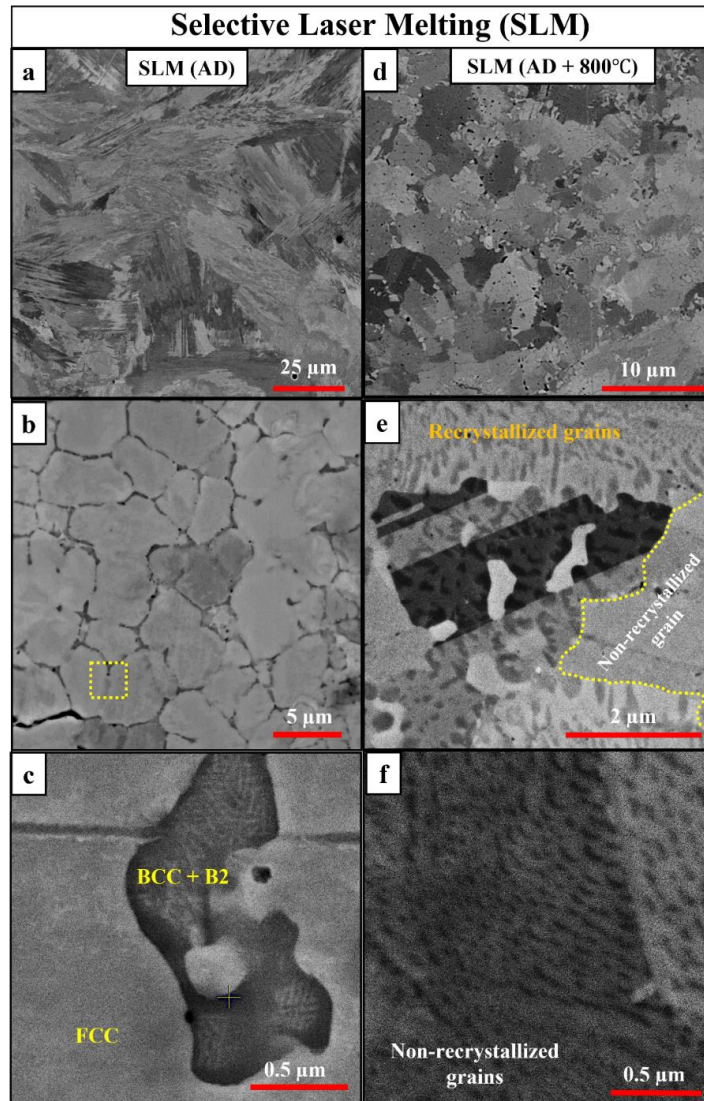

Figure 4: Low, medium, and high magnification SEM backscattered images for (a-c) SLM (AD) and (d-f) SLM (HT or AD+800°C) conditions of SLM processed $Al_{0.3}Ti_{0.2}Co_{0.7}CrFeNi_{1.7}$ HEA.

The SEM backscattered images from the as-deposited (SLM(AD)) and the one-step annealed conditions (SLM(HT)) of the SLM processed $Al_{0.3}Ti_{0.2}Co_{0.7}CrFeNi_{1.7}$ HEA are shown in Figure 4(a-c) and Figure 4(d-f), respectively. The SLM(AD) condition exhibits elongated, possibly growing epitaxially, FCC grains with a significant fraction of solidification cells involving substantial compositional segregation (Figure 4(a-b)). Unlike the DED(AD) condition, the intercellular walls in the SLM(AD) condition exhibited a BCC+B2 microstructure [29]. The high-magnification SEM image of the intercellular region in Figure 4(c) clearly shows the fine-scale B2 precipitates in the darker BCC phase inside the cell wall. The SLM(AD) condition also showed early-stage nanoscale $L1_2$ precipitates within the FCC matrix [29]. The microstructures of the one-step annealed condition, SLM(HT) presented in Figure 4(d-f) appears to be identical to the DED(HT) condition (Figure 3 (d-f)). However, the $L1_2$ precipitates in the SLM(HT) condition are marginally more refined than in the DED(HT) condition. The grain sizes in the as-deposited (~50 μm) and the one-step annealed conditions (~20 μm) are also lower in the case of the SLM-processed alloy as compared to the DED-processed counterpart.

In short, the as-deposited conditions of DED and SLM-processed HEA exhibited predominantly single-phase FCC microstructure with a negligible fraction of $L1_2$ precipitates. Although the SLM(AD) condition revealed B2+BCC microstructure in the intercellular regions between solidification cells, it is shown to have an insignificant effect on the mechanical properties owing to its low phase fraction as well as large separation distances [29]. On the other hand, both heat-treated conditions, SLM(HT) and DED(HT), exhibited hierarchically heterogeneous microstructures at multiple length scales. finer recrystallized FCC grains with rod-like $L1_2$ precipitates and coarser non-recrystallized FCC grains with equiaxed/spherical $L1_2$ precipitates.

Table 8: Nanoindentation Hardness (in GPa) values for all four conditions of AM processed $Al_{0.3}Ti_{0.2}Co_{0.7}CrFeNi_{1.7}$ HEA.

AM method	Condition	RT	250°C	500°C	% Loss
DED	AD	4.157±0.287	3.763±0.212	3.197±0.233	23.13 ↓
	AD+800°C (HT)	4.710±0.123	4.663±0.183	4.387±0.153	6.5↓
SLM	AD	4.116±0.145	3.569±0.171	3.560±0.121	13.3↓
	AD+800°C (HT)	4.654±0.171	4.494±0.132	4.427±0.104	4.9↓

The nanoindentation tests were performed at three different temperatures, RT, 250°C, and 500°C for all four AM processed HEA conditions. The resultant hardness versus temperature plots is presented in Figure 5 and the corresponding hardness values are listed in Table 8. The % loss (reduction) in hardness between the two temperatures, RT and 500°C is calculated for all four conditions using the equation: % loss (reduction) = $\frac{Hardness\ (RT) - Hardness\ (500°C)}{Hardness\ (RT)}$, and the calculated values are listed in the last column of Table 8. The heat-treated conditions (DED(HT) and SLM(HT)) exhibited remarkably higher hardness values (> 4.3 GPa) at all three temperatures compared to the as-deposited conditions of this AM-processed HEA. This increase in the hardness can be attributed to the significantly higher phase fraction of the $L1_2$ precipitates in the heat-treated conditions as opposed to the much lower fractions of precipitates observed in the as-deposited conditions. The anticipated decrease in the hardness with an increase in the temperature from RT to 500°C is observed for all four conditions, as shown in Figure 5. However, the % reduction in the hardness values for the as-deposited conditions (23.1% for DED(AD) and 13.3% for the SLM(AD)) is substantially higher than the heat-treated conditions (6.5% for DED(HT) and 4.9% for SLM(HT)). This large difference in the % reduction in the hardness values can be attributed mainly to two factors: (i) relieving of stored residual stresses in the as-deposited conditions during the high-temperature testing; and (ii) secondly, to

the softer single-phase FCC microstructure compared to the harder hierarchical multi-phase microstructures in the heat-treated conditions. It should be emphasized that the lower values of % reduction in hardness with an increase in temperature in the heat-treated conditions further *signify the stability of the hierarchically heterogeneous microstructures at elevated temperatures*.
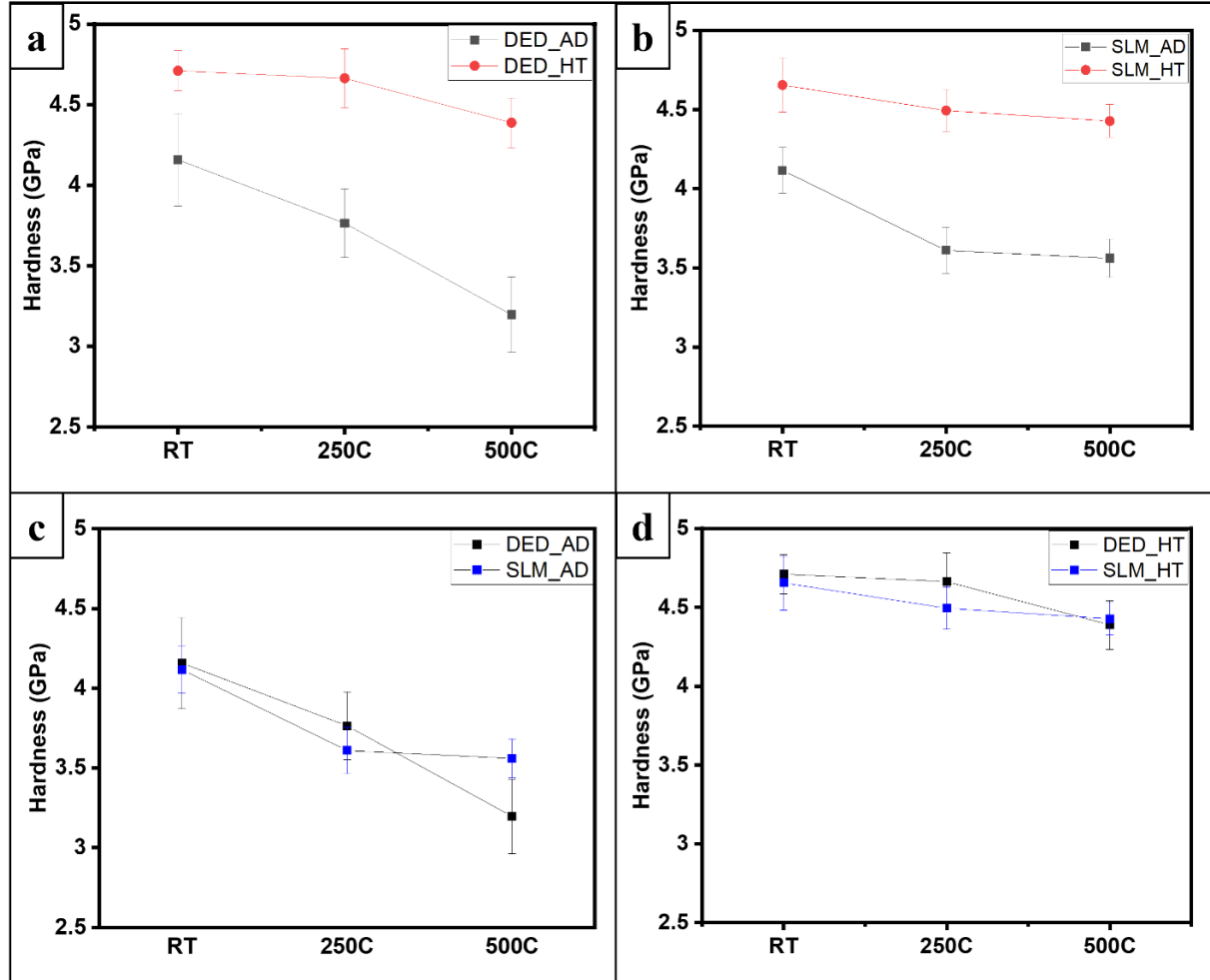

Figure 5: Hardness versus temperature plots comparing (a) DED (AD) and DED (HT) conditions; (b) SLM(AD) and SLM (HT) conditions; (c) DED(AD) and SLM(AD) conditions; and (d) DED(HT) and SLM(HT) conditions of the AM processed $Al_{0.3}Ti_{0.2}Co_{0.7}CrFeNi_{1.7}$ HEA.

While both DED and SLM as-deposited conditions showed nearly identical hardness values at RT, the SLM(AD) condition showed significantly higher hardness than the DED(AD) condition at elevated temperatures, especially at 500°C (Figure 5(c)). However, the heat-treated conditions, DED(HT) and SLM(HT) showed practically overlapping performance at all three temperatures, as shown in Figure 5(d). The load vs. displacement (P-h) curves obtained from the nanoindentation tests for all four conditions are presented in Figure 6. Serrated yielding behavior, also known as Portevin-Le Chatlier (PLC) effect, was observed in the loading portion of the (P-h) curves for the DED(AD) and SLM(AD) conditions tested at 500°C, as shown in Figure 6(c). These perturbations or discontinuities indicate the mechanical instability of the microstructure during the deformation process. The serrated yielding behavior in metals or alloys is commonly associated with the activation of a heterogenous dislocation source and its
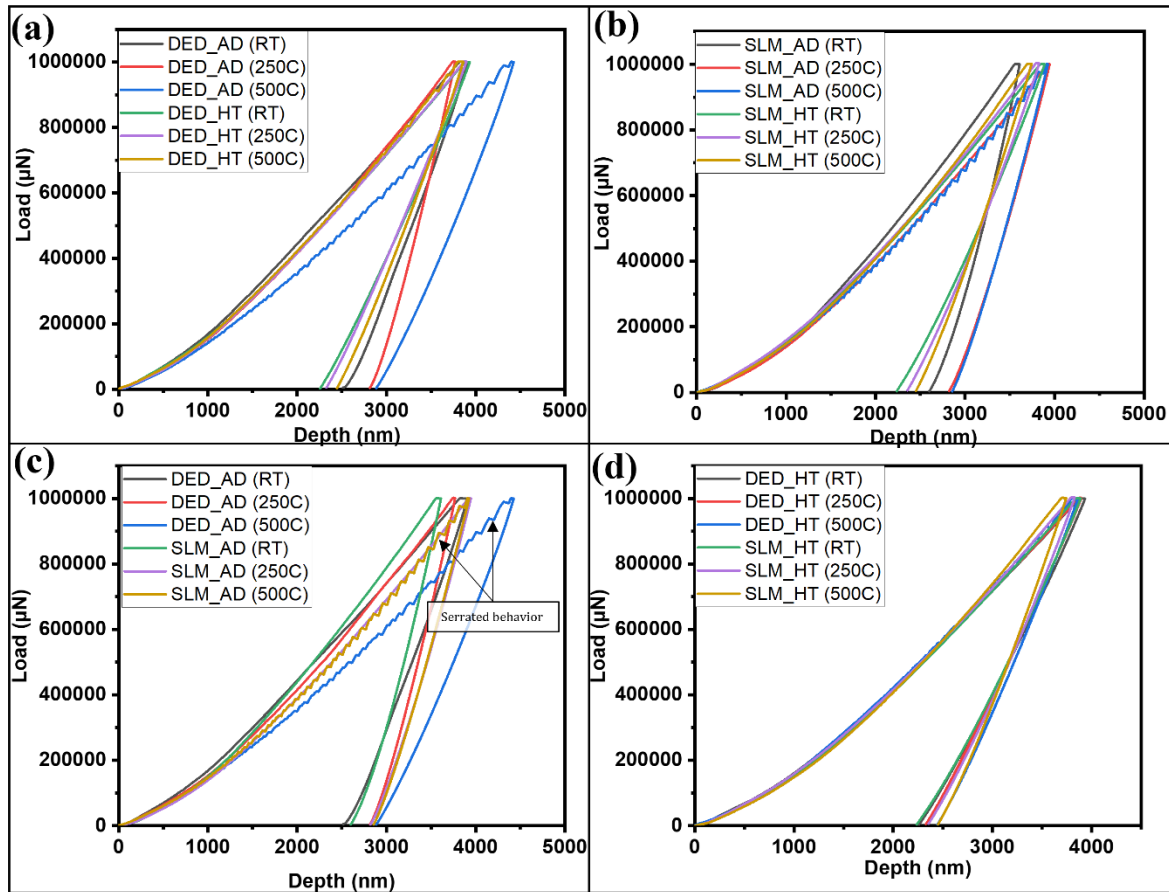
Figure 6: Representative load versus displacement (P-h) curves as a function of temperature comparing (a) DED (AD) and DED (HT) conditions (b) SLM (AD) and SLM(HT) conditions (c) DED(AD) and SLM(AD) conditions and (d) DED(HT)and SLM(HT) conditions, $Al_{0.3}Ti_{0.2}Co_{0.7}CrFeNi_{1.7}$ HEA.

multiplication under loading [221]. However, Schuh's [222] review on "Nanoindentation studies of materials" additionally points out that phase transformations that occur during the nanoindentation process could also result in the serrated yielding or the PLC effect [223]. Therefore, microstructural characterization was performed on DED(AD) and SLM(AD) conditions post-nanoindentation (at 500°C), and the resultant SEM backscattered images are presented in Figure 7(a,b) and Figure 7(c,d), respectively. Features resembling $L1_2$ precipitates were present in both conditions, demonstrating the possibility of dynamic precipitation of the $L1_2$ phase within the FCC matrix during the nanoindentation testing at 500°C. Moreover, the phase fraction versus temperature prediction for this HEA ($Al_{0.3}Ti_{0.2}Co_{0.7}CrFeNi_{1.7}$) presented in Figure 8 revealed almost 40% for the $L1_2$ phase at 500°C. It is envisaged that dynamic precipitation pins down the mobile dislocations, restoring the hardness locally during the deformation [224,225] Therefore, the serrated yielding observed in the DED(AD) and SLM(AD) conditions during the nanoindentation loading (at 500°C) could be mainly due to the precipitation of the $L1_2$ phase within the FCC matrix.

It should be noted that the same serrated behavior is not observed for SLM(AD) or DED(AD) conditions tested at RT or 250°C (Figure 6(c)). The phase fraction versus temperature plot (in Figure 8) reveals no significant change in the $L1_2$ phase fraction for temperatures below 500°C.

Therefore, it is intuitive that sluggish diffusion at lower temperatures makes the $L1_2$ precipitation kinetically unfavorable. Hence, no serrations were observed in the P-h curves for DED(AD) and SLM(AD) conditions tested at RT and 250°C. Similarly, the P-h curves in Figure 6(d) for DED(HT) and SLM(HT) conditions did not reveal any signs of serrated yielding during nanoindentation, which *again illustrates the stability of the hierarchically heterogeneous microstructures during deformation at elevated temperatures.*
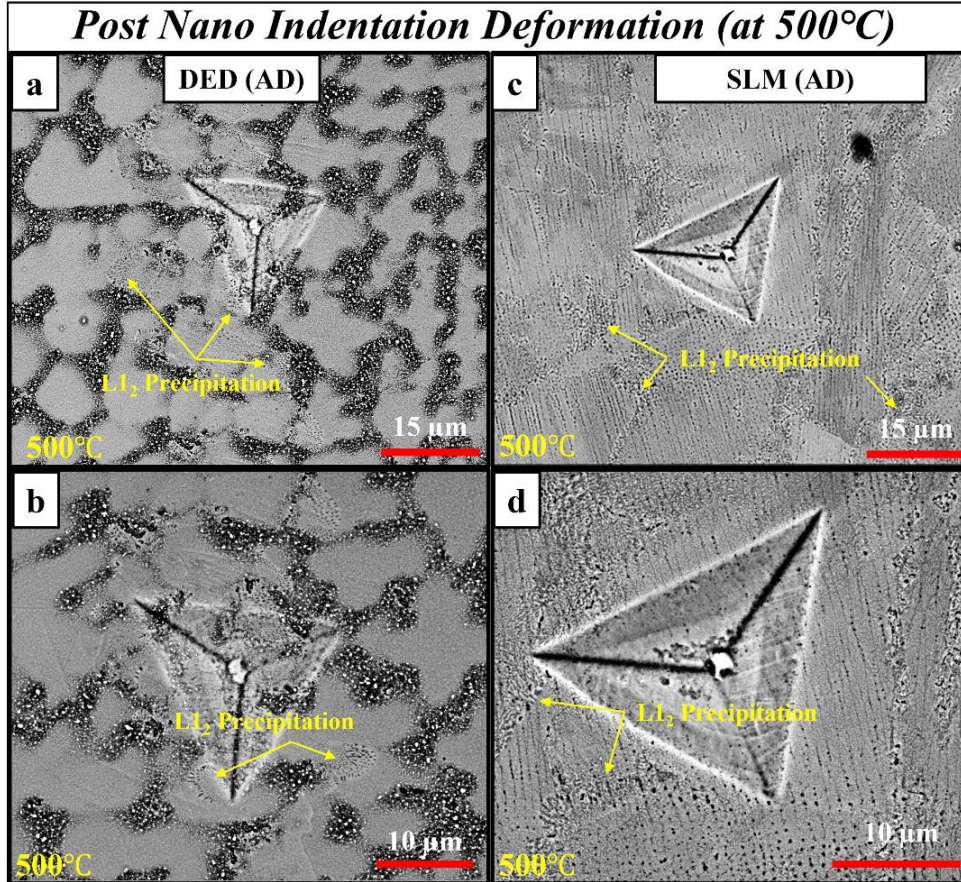

Figure 7: SEM backscattered Images revealing the $L1_2$ precipitation post nano-indentation deformation at 500°C for (a,b) DED (AD) and (c,d) SLM(AD) conditions of the AM processed HEA.
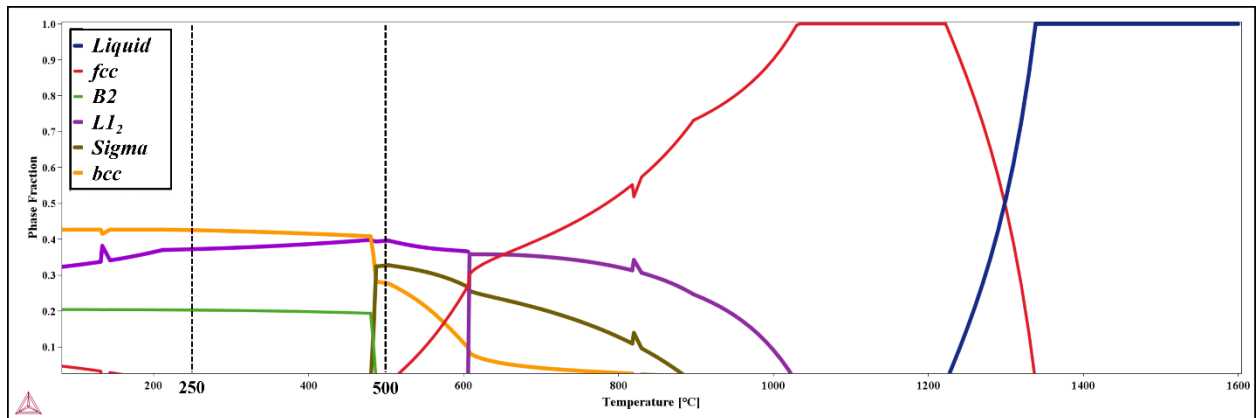

Figure 8: Phase fraction vs temperature plot for $Al_{0.3}Ti_{0.2}Co_{0.7}CrFeNi_{1.7}$ high- entropy alloy (HEA) generated using Thermo-Calc software.

4.1.4   Summary

In summary, the temperature-dependent (from RT to 500°C) nanoindentation behavior of the DED and SLM processed $Al_{0.3}Ti_{0.2}Co_{0.7}CrFeNi_{1.7}$ HEA was investigated in the as-deposited and one-step annealed conditions for this study. The hierarchically heterogeneous microstructures obtained via simple one-step annealing of the DED and SLM-processed HEA exhibited significantly better performance than the nearly homogeneous microstructures in the as-deposited state. The one-step annealed conditions revealed less than 6.6% reduction in hardness values at 500°C compared to RT, while the as-deposited conditions showed greater than 18% reduction in hardness between RT and 500°C. The one-step annealed conditions also exhibited significantly higher hardness than the as-deposited conditions owing to their multi-phase (FCC+$L1_2$) microstructures with a substantial fraction of ordered $L1_2$ precipitates. Furthermore, serrated yielding (PLC effect) indicative of microstructural instability was observed during nanoindentation deformation (at 500°C) for both SLM and DED processed conditions but not after the one-step annealing. Overall, the nanoindentation results signify the stability of these hierarchically heterogeneous microstructures developed via single step annealing, exploiting the residual stresses in the AM processed $Al_{0.3}Ti_{0.2}Co_{0.7}CrFeNi_{1.7}$ HEA. The results presented in this study open strong possibilities for applications of HEAs in high-temperature nuclear reactors. As mentioned in Table 7, ShAPE processing followed by high-temperature nano-indentation testing at 800°C is in progress.

4.2   Down selected HEA: $Al_{10}Cr_{12}Fe_{35}Mn_{23}Ni_{20}$

4.2.1   Background

According to the U.S. Nuclear Regulatory Commission report titled "Use of High Entropy Alloys (HEAs) in Future Nuclear Applications" published in January 2023, three HEAs ($Al_{0.3}Cu_{0.5}CrFeNi_2$, $Al_5Cr_{12}Fe_{35}Mn_{28}Ni_{20}$ and $Al_{10}Cr_{12}Fe_{35}Mn_{23}Ni_{20}$) exhibited enhanced structural and functional properties over the code certified materials. Further, the report identifies AlCuCrFeNi and AlCrFeMnNi HEAs as compositional areas of interest for future studies. Among these three HEAs, $Al_{10}Cr_{12}Fe_{35}Mn_{23}Ni_{20}$ has the highest YS and UTS, and therefore has been chosen for experimental work in the current work package. Cast rods of this HEA were procured from sophisticated alloys and ShAPE processing followed by nanoindentation testing is in progress.

4.3   Graded High Entropy Alloys

4.3.1   Background

In nuclear reactor environments, where the materials are subjected to thermal and mechanical stresses, corrosion, diffusion and irradiation, development of advanced coatings may prevent the materials from these degradation mechanisms. Novel materials and associated advanced manufacturing techniques for coatings along with advanced characterization are required for improvement of coatings performance. FeCoCrNi based HEAs can present a single-phase FCC structure that demonstrates superior irradiation resistance compared to multi-phase and BCC structures. Previous studies have revealed that there are significant challenges in manufacturing the single phase HEAs with conventional casting methods.

This work utilizes DED AM as a coating materials development technology that allows the fabrication of graded HEAs. LENS DED is uniquely suited to tailor material properties and

compositions to a specific application and features a high control over processing parameters that allows for microstructural and as-built optimization. The DED method can control flow of powders during fabrication to result in a component with gradual variation of chemistry along the build direction and resulting in compositionally graded materials. This compositional variation also alters the inherent microstructure with changes in phase fraction, mechanical properties etc. Hence, a proper design of coatings can be developed that benefits from spatial variation in properties.

4.3.2   Materials and Methods

The graded HEA composition was fabricated using DED method in a Optomec® LENS MR-7 equipment at Idaho National Laboratory (INL) as part of a INL LDRD (2019-2021). The three alloy powders for mixing were 70Co30Cr (commercially known as Stellite 21), 316L stainless steel and IN 718 alloy, and specimens of 10 layer of compositions were fabricated to create graded materials.

In the INL's LDRD program, microstructural characterization on graded sections of materials was performed using SEM and compositional changes across the build were determined using EDS [226]. Nanoindentation was performed across the build direction to identify trends along complex sample compositions. Bulk cross-sections were assessed for successful fusion and lack of macroscopic defects (unmelted particles, separation of layers, etc.) [227]. However, microscopic inhomogeneous regions including unmelted powders and agglomerated elements (e.g., CoCr) were observed in optical and SEM imaging. The motivation of this work is to understand the details of such regions and adjacent HEA regions using TEM. A thorough understanding of such region chemistry and formation mechanism will help in optimization of printing parameters (adjust hatch spacing, energy density, potentially dynamic process parameter adjustment) to increase homogeneity and performance [228].

A Helios Hydra Plasma focused ion beam (FIB) was used to prepare the TEM lamella. A JEOL Grand Arm scanning TEM (STEM) with a Schottky field emission gun operated at 300 keV was used for nanoscale characterization of samples microstructure. The high-angle annular dark-field TEM/STEM imaging was used to analyze the samples. High-resolution elemental mapping was also acquired using X-ray energy dispersive spectrometry in STEM mode.

4.3.3   Results and Discussion

Figure 9(a) shows the schematic of the gradient HEA sample that was DED fabricated using powders of three different off-shelf powders upon the substate of 316L alloy. The schematic shows the build layers with thickness in a range of 0.3 – 0.5 mm. The content of CoCr, IN718, and 316L powder vary along the build direction with each layer. Fig. 9(b) shows the photograph of the graded sample on the top of the substrate as marked by the yellow line. Fig. 9(c) shows the optical image of the substrate and the graded material, and the layers of deposition are visible by the image contrast. The microscopic pores are also visible that are commonly observed in AM materials. Figure 9 (d) shows the chemical map generated by EDS in SEM that clearly shows the compositional variation of primary elements, such as Fe, Co, and Cr along the build direction. Figure 9 (e) shows an enlarged optical image of the region marked in the fifth box of Figure 9 (c). This area contained a possible unmelted agglomeration of Fe rich region. Further, a TEM lamella was prepared in the region indicated by the green box for nanoscale analysis of the interface of the HEA and the unmelted region.
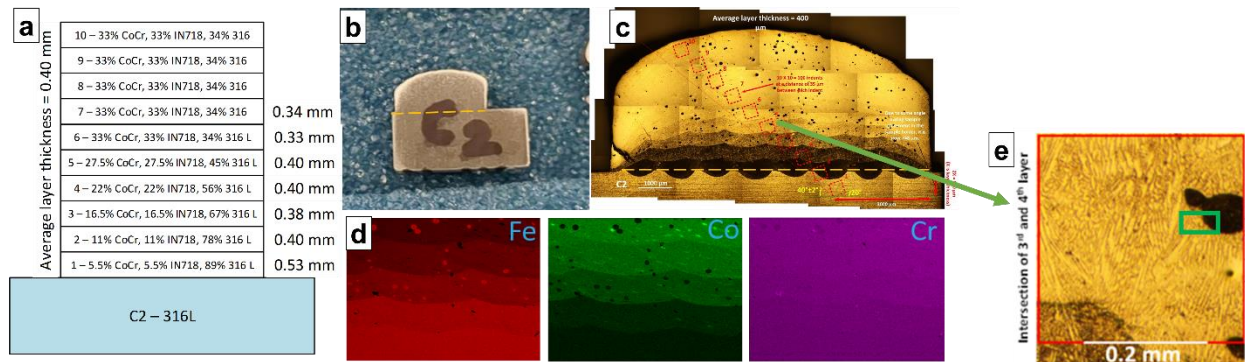
Figure 9: (a) A schematic of the gradient HEA composition fabrication upon the 316L substrate using DED method; (b) the fabricated gradient material on the substrate, demarked by the yellow line; (c) the optical image of the gradient materials; (d) SEM images show the continuous variation of Fe, Co, and Cr with deposition thickness; and (e) an enlarged optical image showing the area of interest and the marked as region "5" in (c). The approximate area of TEM lift-out has been marked in the green box.

Figure 10(a) shows the pre-final FIB lift out where the interface between the unmelted region and the HEA region is clear visible and has been marked by the red line. Figure 10(b) shows the STEM image of the region where the small precipitates on both sides of interface are visible. Figure 10(c) shows the chemical map generated by the EDS in TEM that clearly shows the Co compositional variation across these two regions. Apart from Co, Fe appears to be higher in the unmelted region. So, it is possible that it can be unmelted 316L powder. Similarly, Figure 10(d-g) shows the chemical maps of Fe, Ti, Cr, and Ni respectively. One of the precipitates in the HEA region has been identifies as Ti-rich in Figure 10(e) while the unmelted part has Cr rich precipitates in shown in Figure 10(f).
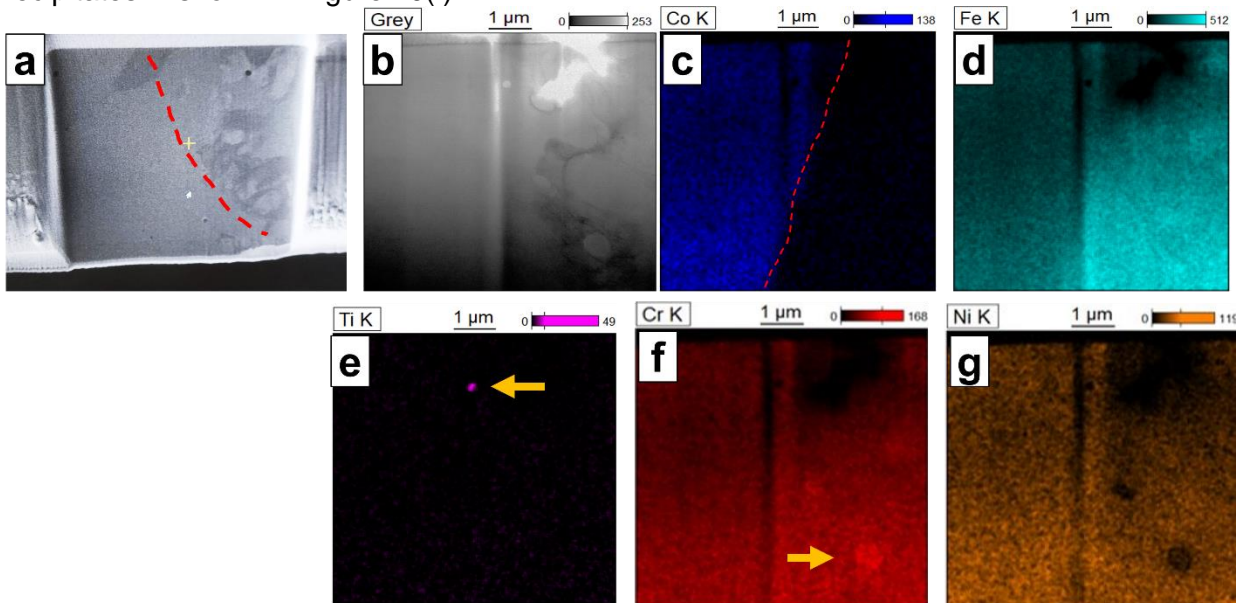

Figure 10: (a) The FIB lift-out shows the area of interest showing the unmelted steel powder on the left side; (b) the STEM image shows the same of interest with the interface between the HEA and the unmelted steel powder particle; (c) the Co elemental map shows interface between the

two phases. The Ti map in (e) shows the Ti-rich region in HEA region and (f) shows the Cr rich region in unmelted steel powder particle.

Figure 11 focuses on the HEA region highlight the chemistry of the precipitate phase. The precipitate in HEA side is further studied and it has been identified as Ti oxide based on the strong presence of Ti and O, as shown in Figure 11(c-d). Usually, Ti has been reported to form oxide readily during powder processing. But it is not determined whether the oxide was already present in the powder used or formed during processing. However, only one of such oxide particles is observed in the TEM lamella, so it can be believed that the volume fraction of such oxide inclusion is very low.
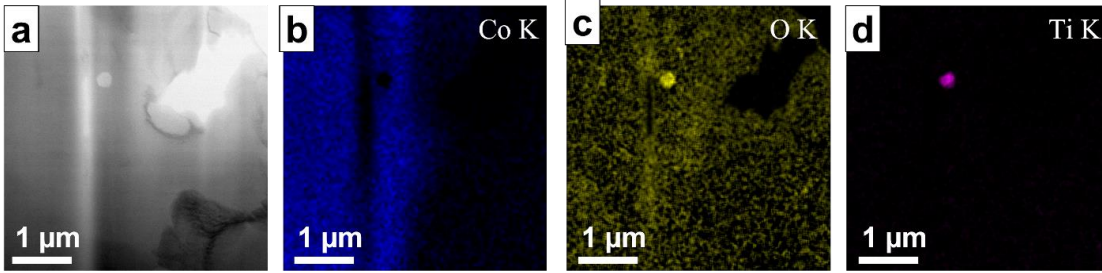
Figure 11: (a) The STEM image shows the morphology of the Ti oxide precipitate in the HEA region. The chemical maps in the HEA region highlight the Ti and O presence in the form of the precipitate in (b – d).

Similarly, Figure 12 shows the unmelted region that was further analyzed to identify the composition of precipitates present in this region. Figure 12(a) shows the spherical precipitate and the Figure 12(b-e) shows the individual chemical map in the region. The precipitate appears to be strongly rich in Cr.
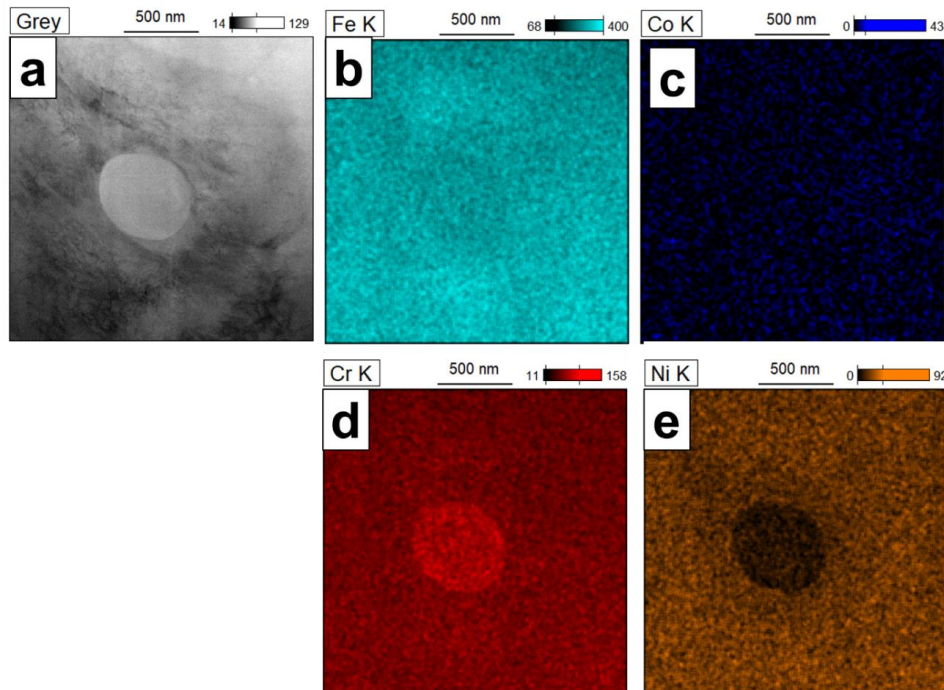
Figure 12: (a) The STEM image shows the morphology of the Cr-rich particle in the unmelted steel; (b-d) shows the elemental distribution in the Cr rich region.

Figure 13(a) shows a SEM image of the HEA region that shows the formation of dendritic and interdendritic region during the solidification process. The interdendritic regions appear to be mostly a continuous channel but there are some regions where they appear to be discontinuous. It is possibly due to the projection of the interdendritic channels running within the sample and not being captured in such two-dimensional images. The same dendritic-interdendritic has been observed in TEM as well in the HEA region, as shown in Figure 13(b). Further Chemical analysis in Figure 13(c-g) shows that the interdendritic region is mostly enriched in Nb. It also corresponds to the brighter chemical contrast of interdendritic region as seen in Figure 13(a).
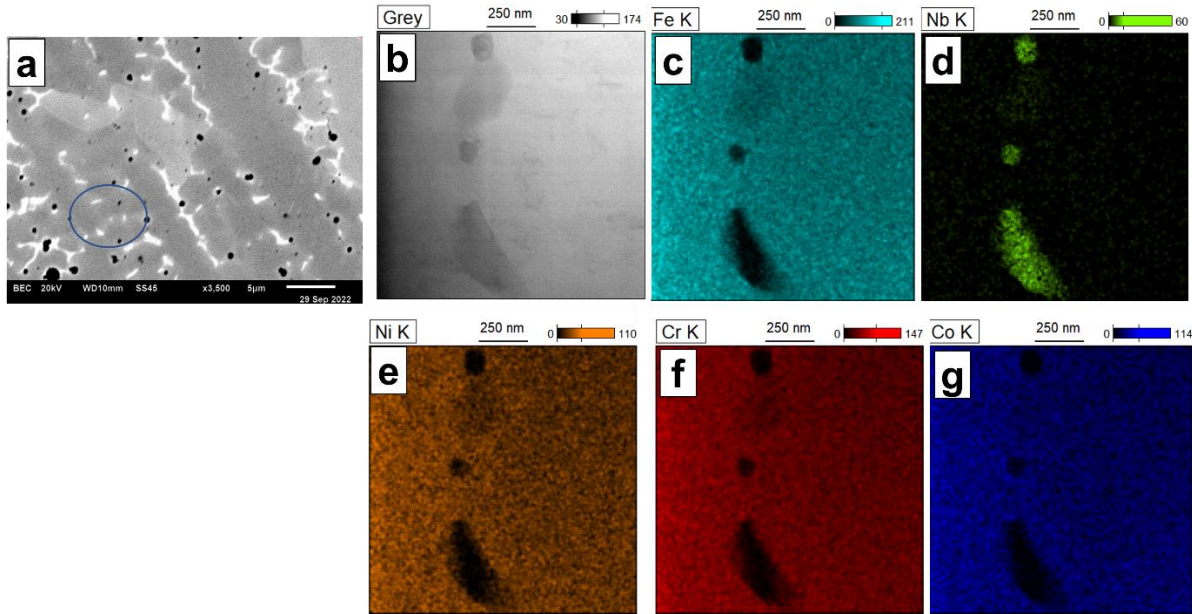
Figure 13: (a-b) a SEM and STEM image show the dendritic-interdendritic region formation in the HEA region; (c-g)) the chemical map using STEM-EDS shows the strong presence of Nb and absence of Fe, Ni, Cr, Co in the interdendritic region.

4.3.4   Summary

A novel DED fabrication of graded compositions of HEAs using off-the-shelf common alloy powders has been studied using advanced microscopy. The main findings are mentioned below:

a) The composition in each build layer appears to be quite homogeneous. The HEA seems to form dendritic-interdendritic region mainly due to presence of element, such as Nb.

b) The HEA still contains some unmelted parts of possible 316L powders. The unmelted region has been examined and it contained nanoscale Cr rich precipitates.

c) The HEA region also contains a small fraction of Ti oxide precipitates.

Although the microstructural examination confirms the successful fabrication of graded materials, further optimization of process parameters is needed to reduce porosity in the microstructure and undesired brittle intermetallic phases.

5.0 Research Outcomes

- The work performed under this work package will be presented in the accepted talks at the following conferences:

  - **International Conference on Additive Manufacturing (ICAM) 2023, October 30 – November 3rd, 2023**
    - o **Title:** HEAs for Nuclear Energy Applications and Potential Advanced Manufacturing Methods
    - o **Authors:** *Mohan Sai Kiran Kumar Yadav Nartu,* Isabella van Rooyen (PNNL), Rajarshi Banerjee (UNT)
    - o **Location:** Washington, D.C
    - o **Date:** November 1, 2023

  - **3rd World Congress on High Entropy Alloys (HEA 2023), November 12 – 15th, 2023**
    - o **Title:** Development of High Entropy Alloy based Coatings via Directed Energy Deposition (DED) Additive Manufacturing for Nuclear Applications
    - o **Authors:** *Subhashish Meher*, Mohan Nartu, Chinthaka Silva, Isabella van Rooyen (PNNL), Calvin Downey, Luis Nunez (INL), Michael Maughan, Yogesh Sighla (University of Idaho)
    - o **Location:** Pittsburgh, PA
    - o **Date:** November 15, 2023

  - **Materials in Nuclear Energy Systems (MiNES 2023), December 10 – 14th, 2023**
    - o **Title:** Engineering heterogeneous microstructures in Additively Manufactured $Al_{0.3}Ti_{0.2}Co_{0.7}CrFeNi_{1.7}$ High Entropy Alloy for potential nuclear applications
    - o **Authors:** *Mohan Sai Kiran Kumar Yadav Nartu*, Isabella van Rooyen (PNNL), Shristy Jha, Advika Chesetti, Sundeep Mukherjee, Rajarshi Banerjee (UNT)
    - o **Location:** New Orleans, LA

- A part of the work is under consideration for publication in the TMS journal, *JOM, December 2023 edition*.
    - o **Title:** Microstructure and Temperature Dependent Indentation Response of Additively Manufactured Precipitation-strengthened Al0.3Ti0.2Co0.7CrFeNi1.7 High Entropy Alloy.
    - o **Authors**: *Mohan Sai Kiran Kumar Yadav Nartu*, Shristy Jha, Advika Chesetti, Sundeep Mukherjee, Isabella van Rooyen, and Rajarshi Banerjee

6.0 Preliminary Decision Matrix Rating of two Down selected HEAs

Based on the literature review, the preliminary experiments performed, and engineering rational, a preliminary rating was performed on the two down selected alloys and summarized in Table 9 with the associated justification below in the text. HEA $Al_{10}Cr_{12}Fe_{35}Mn_{23}Ni_{20}$ performed marginally better than HEA $Al_{0.3}Ti_{0.2}Co_{0.7}CrFeNi_{1.7}$ with a rating of 62.5 vs 56.5.

Table 9: Preliminary decision matrix rating

	Criteria	$Al_{0.3}Ti_{0.2}Co_{0.7}CrFeNi_{1.7}$	$Al_{10}Cr_{12}Fe_{35}Mn_{23}Ni_{20}$
Application Space	Applicability to Different Reactor Types	3	5
	Other Industry Experience	3	3
	Data Availability	0	0
	Code & Standards Availability	0	0
	Component Versatility	2	2
Environmental Compatibility	Radiation Resistance	0	0
	Elemental Transmutation	0	0
	High Temperature Oxidation Resistance	0	0
	Neutronics Compatibility	0	0
	Coolant Compatibility & Corrosion Resistance	0	0
Physical & Mechanical Properties	Thermal Conductivity	0	0
	Thermal Capacity	0	0
	Tensile Properties	5	5
	Creep Performance	0	0
	Fatigue	0	0
	Fracture Toughness	0	3
	Microstructural Dependency	5	5
	Scope for Microstructural Enhancement	5	5
Manufacturability	Reproducibility/Consistency	4	4
	Process Complexity	4.5	4.5
	Cost	3	3
	Scalability	5	5
	Production Method TRL	1	1
	Raw Material Supply	3	5
	Flexibility of Manufacturing	5	5
	Conventional Machining	3	3
	Near Net Shaping (Complexity of Shape)	5	4
	Overall Scores	56.5	62.5

6.1 Justification of ratings

6.1.1 $Al_{0.3}Ti_{0.2}Co_{0.7}CrFeNi_{1.7}$

$Al_{0.3}Ti_{0.2}Co_{0.7}CrFeNi_{1.7}$ High Entropy Alloy was given a score of 56.5 out of possible 135 based on the decision criteria matrix. Most of criteria scored "0" as this HEA is recently developed and have no data reported for those criteria particularly. However, some of the criteria have been assigned a score based on limited data available in the literature. The justification for the assigned scores is provided below.

Applicability to Different Reactor Types (3/5):

The mechanical and functional properties of $Al_{0.3}Ti_{0.2}Co_{0.7}CrFeNi_{1.7}$ HEA can be significantly tuned to withstand the environments in several reactors. Moreover, this HEA is believed to retain its structural integrity up to 1100℃. Since, there is no experimental data available on the application of this HEA in any of the reactors yet, a score of 3 can been assigned based on intuition.

Other Industry Experience (3/5):

HEAs are typically suitable for structural applications and hence a widespread use in various other industries is envisaged. Since there are no reports investigating the other industry application, a score of 3 has been assigned.

Component Versatility (2/5):

This HEA has foreseen application as a fuel cladding material requiring good structural integrity. Other applications may open after determining this HEA's properties in other aspects such as corrosion, irradiation resistance, etc. Therefore, only a score of 2 has been assigned.

Tensile Properties (5/5)

This HEA is reported to exhibit a yield strength of ~1630 MPa, and good tensile ductility of ~15% at room temperature, which is significantly higher than most Stainless Steels. This HEA is expected to have high-temperature stability up to ~1100°C, hence a score of 5 has been assigned for tensile properties.

Microstructural Dependency (5/5)

The mechanical and functional properties of this HEA are greatly dependent on the underlying microstructure, therefore a score of 5 has been assigned.

Scope for Microstructural Enhancement (5/5)

Since this HEA's properties can be significantly tuned, a score of 5 has been assigned.

Reproducibility/Consistency (4/5)

This HEA has only been manufactured via Casting, Directed Energy Deposition and Selective Laser Melting so far. While, Casting is highly reproducible and consistent, the other two laser additive manufacturing techniques may not be and needs further validation. Therefore, a score of 4 has been assigned.

Process Complexity (4.5/5)

This HEA can be easily manufactured via Casting or Additive Manufacturing. However, Additive Manufacturing involves a preprocessing step of producing good quality spherical powders prior which are chiefly made via atomization process. Therefore, a score of 4.5 is assigned.

Cost (3/5)

Since this HEA is not commercially produced yet, a score of 3 has been assigned as the cost would be comparable to any stainless steels produced commercially today.

Scalability (5/5)

The scalability for this HEAs is only limited by the type of processing technique employed and no specific issues pertaining to its composition is foreseen and therefore a score of 5 can be assigned.

Production level TRL (1/5)

This HEA is not commercially produced yet, and only a handful of research articles can be found. Therefore, a score of 1 has been assigned.

Raw Material Supply (3/5)

The raw material supply for casting of this HEA should be no different from any stainless steels. However, for Additive Manufacturing the availability of HEA powders can be highly challenging. Therefore, a score of 3 has been assigned.

Flexibility of Manufacturing (5/5)

This HEA can be manufactured via all the bulk manufacturing techniques and hence a score of 5 has been assigned.

Conventional Machining (3/5)

The part if manufactured via casting requires significant post processing but requires only requires minimal post processing when fabricated via Additive Manufacturing. Therefore, an average score of 3 has been assigned.

Near Net Shaping (Complexity of Shape) (5/5)

The fabrication of this HEA is not limited by the complexity of the design.

6.1.2 $Al_{10}Cr_{12}Fe_{35}Mn_{23}Ni_{20}$

$Al_{10}Cr_{12}Fe_{35}Mn_{23}Ni_{20}$ High Entropy Alloy was given a score of 62.5 out of possible 135 based on the decision criteria matrix. Most of criteria scored "0" as this HEA is recently developed and have no data reported for those criteria particularly. However, some of the criteria have been assigned a score based on limited data available in the literature. The justification for the assigned scores is provided below.

Applicability to Different Reactor Types (5/5):

$Al_{10}Cr_{12}Fe_{35}Mn_{23}Ni_{20}$ HEA is free from cobalt and moreover the properties can be greatly tuned to withstand the environments in several reactors. Despite, no experimental data available on the application of this HEA in any of the reactors yet, the NRC report strongly recommends this HEA for future nuclear applications due to its enhanced mechanical properties and microstructural benefits, therefore a score of 5 has been assigned.

Other Industry Experience (3/5):

HEAs are typically suitable for structural applications and hence a widespread use in various other industries is envisaged. Since there are no reports investigating the other industry application for this HEA, a score of 3 has been assigned.

Component Versatility (2/5):

This HEA has foreseen application as a fuel cladding material requiring good structural integrity. Other applications may open after determining this HEA's properties in other aspects such as corrosion, irradiation resistance, etc. Therefore, only a score of 2 has been assigned.

Tensile Properties (5/5)

This HEA in cold rolled state is reported to exhibit a yield strength of ~1400 MPa, and decent tensile ductility of ~5.83% at room temperature, which is significantly higher than most Code Certified Materials. Hence a score of 5 has been assigned for tensile properties.

Fracture Toughness (3/5)

The fracture toughness of this HEA in the cold rolled state is ~ 79 MPa√m which is slightly lower than other code certified materials, therefore a score of 3 has been assigned.

Microstructural Dependency (5/5)

The mechanical and functional properties of this HEA are greatly dependent on the underlying microstructure, therefore a score of 5 has been assigned.

Scope for Microstructural Enhancement (5/5)

Since this HEA's properties can be significantly tuned, a score of 5 has been assigned.

Reproducibility/Consistency (4/5)

This HEA has been manufactured via casting which is highly reproducible and consistent. Therefore, a score of 5 has been assigned.

Process Complexity (4.5/5)

This HEA can be easily manufactured via Casting without any preprocessing required. Therefore, a score of 5 is assigned.

Cost (3/5)

Since this HEA is not commercially produced yet, a score of 3 has been assigned as the cost would be comparable to any stainless steels produced commercially today.

Scalability (5/5)

The scalability for this HEAs is only limited by the type of processing technique employed and no specific issues pertaining to its composition is foreseen and therefore a score of 5 can be assigned.

Production level TRL (1/5)

This HEA is not commercially produced yet, and only a handful of research articles can be found. Therefore, a score of 1 has been assigned.

Raw Material Supply (5/5)

The raw material supply for casting of this HEA should be no different from any stainless steels. Therefore, a score of 5 has been assigned.

Flexibility of Manufacturing (5/5)

This HEA can be manufactured via all the bulk manufacturing techniques and hence a score of 5 has been assigned.

Conventional Machining (3/5)

The part if manufactured via casting requires significant post processing but requires only requires minimal post processing when fabricated via Additive Manufacturing. Therefore, an average score of 3 has been assigned.

Near Net Shaping (Complexity of Shape) (4/5)

The fabrication of this HEA is not limited by the complexity of the design. However, the presence of element Cu in the HEA may pose some processing challenges via laser additive manufacturing. Therefore, a score of 4 has been assigned.

7.0 Conclusion and Recommendation

The HEA classification used in this review and the elaborate literature survey presented in this report provide insights into the processing, microstructure, and properties of the several HEAs reported targeting different applications. Based on the literature survey, six HEA's were identified as promising for the nuclear industry focusing on the high temperature properties with Co as an alloying element in two of these alloys $((Ni_2Co_2FeCr)_{92}Al_4Nb_4; Al_{0.3}Ti_{0.2}Co_{0.7}CrFeNi_{1.7})$. GRX-810, developed by NASA shows creep performance 2-3 orders of magnitude better than the current high temperature alloys, is best classified as a medium entropy alloy or an ODS alloy due to the presence of Y_2O_3 particles and therefore, we recommend pursuing this material as part of a different AMMT work package. Although the decision matrix is not fully developed yet for the six candidate HEA's, the literature survey provides technical justification to down select two HEAs ($Al_{0.3}Ti_{0.2}Co_{0.7}CrFeNi_{1.7}$ and $Al_{10}Cr_{12}Fe_{35}Mn_{23}Ni_{20}$) for detailed experimental work under this work package. This work package also investigated an advanced processing route for fabricating functionally graded HEAs using DED and off-the-shelf metal alloy powders. This advanced processing methodology for functionally graded HEAs would open avenues for rapidly assessing new HEA compositions at significantly cheaper costs.

Most of the HEA research used arc (73%) and vacuum melting (15%) processes as a fabrication method, with only 11% of the papers reviewed used laser based additive manufactured processes. Solid state manufacturing processes were only reported in less than 5% of the instances. The literature survey shown therefore the opportunity to explore solid phase processes as a manufacturing technique due to the grain refinement and decreased segregation properties during processes. Therefore, the inclusion of ShAPE is in progress for the two down-selected HEAs ($Al_{0.3}Ti_{0.2}Co_{0.7}CrFeNi_{1.7}$ and $Al_{10}Cr_{12}Fe_{35}Mn_{23}Ni_{20}$) due to its unique processing conditions which result in finer microstructures with compositionally homogenous grains that would potentially enhance the mechanical properties. In addition, the effect of solid phase processing on the mechanical properties of a single-phase HEA can also provide valuable information and potential more economical routes to HEA adoption to the markets. It is therefore also recommended that a functional graded alloy to HEA as a final coating be explored to determine the impact on the interlayers and interface properties.

The temperature-dependent (from RT to 500°C) nanoindentation behavior of the DED and SLM processed $Al_{0.3}Ti_{0.2}Co_{0.7}CrFeNi_{1.7}$ HEA was investigated in the as-deposited and one-step annealed conditions for this study. The hierarchically heterogeneous microstructures obtained via simple one-step annealing of the DED and SLM-processed HEA exhibited significantly better performance than the nearly homogeneous microstructures in the as-deposited state. The one-step annealed conditions revealed less than 6.6% reduction in hardness values at 500°C compared to RT, while the as-deposited conditions showed greater than 18% reduction in hardness between RT and 500°C. The one-step annealed conditions also exhibited significantly higher hardness than the as-deposited conditions owing to their multi-phase (FCC+$L1_2$) microstructures with a substantial fraction of ordered $L1_2$ precipitates. Furthermore, serrated yielding (PLC effect) indicative of microstructural instability was observed during nanoindentation deformation (at 500°C) for both SLM and DED processed conditions but not after the one-step annealing. Overall, the nanoindentation results signify the stability of these hierarchically heterogeneous microstructures developed via single-step annealing, exploiting the residual stresses, in the AM-processed $Al_{0.3}Ti_{0.2}Co_{0.7}CrFeNi_{1.7}$ HEA. Overall, the results presented were promising. However, applying this HEA in high-temperature nuclear reactors would require a more detailed assessment of other properties. ShAPE processing followed by

high-temperature, nano-indentation testing at 800°C is in progress. This HEA is also expected to have high-temperature stability up to ~1100 °C.

Microstructural characterization of the graded compositions of HEAs fabricated via DED technique using off-the-shelf common alloy powders has been performed. The results reveal homogenous compositions in each build layer. However, the graded HEAs formed dendritic-interdendritic microstructures mainly due to the presence of heavier elements, such as Nb. Few regions contained unmelted 316 L powders with nano-scale Cr rich precipitates sparsely distributed. Additionally, Ti-oxide particles were observed in the HEA matrix. While the microstructural examination indicates the successful fabrication of graded materials, further investigation is needed to optimize the process parameters to reduce porosity and undesired brittle intermetallic phases and ensure complete melting of the metal alloy powders.

Based on the literature review, the preliminary experiments performed, and engineering rational, a preliminary rating was performed on the two down selected alloys. HEA $Al_{10}Cr_{12}Fe_{35}Mn_{23}Ni_{20}$ performed marginally better than HEA $Al_{0.3}Ti_{0.2}Co_{0.7}CrFeNi_{1.7}$ with a rating of 62.5 vs 56.5.

The research performed as part of this study, resulted in 3 conference presentations and one accepted journal publication.

8.0 References

1. E. J. Pickering, A. W. Carruthers, P. J. Barron, S. C. Middleburgh, D. E. J. Armstrong, and A. S. Gandy, Entropy 2021, Vol. 23, Page 98 **23**, 98 (2021).
2. O. El-Atwani, N. Li, M. Li, A. Devaraj, J. K. S. Baldwin, M. M. Schneider, D. Sobieraj, J. S. Wróbel, D. Nguyen-Manh, S. A. Maloy, and E. Martinez, Sci Adv **5**, (2019).
3. A. S. Gandy, B. Jim, G. Coe, D. Patel, L. Hardwick, S. Akhmadaliev, N. Reeves-McLaren, and R. Goodall, Front Mater **6**, (2019).
4. A. Ayyagari, R. Salloom, S. Muskeri, and S. Mukherjee, Materialia (Oxf) **4**, 99 (2018).
5. O. A. Waseem and H. J. Ryu, Sci Rep **7**, (2017).
6. T. Nagase, S. Anada, P. Rack, J. Noh, H. Y.- Intermetallics, and undefined 2012, Elsevier (n.d.).
7. T. Nagase, S. Anada, P. Rack, J. Noh, H. Y.- Intermetallics, and undefined 2013, Elsevier (n.d.).
8. S. Q. Xia, X. Yang, T. F. Yang, S. Liu, and Y. Zhang, JOM **67**, 2340 (2015).
9. T. Nagase, P. Rack, J. Noh, T. E.- Intermetallics, and undefined 2015, Elsevier (n.d.).
10. S. Xia, W. Zhen, T. Yang, Y. Z.-J. of I. and S. Research, and undefined 2015, Elsevier (n.d.).
11. S. Middleburgh, … D. K.-R. S. open, and undefined 2015, Royalsocietypublishing.Org **2**, (2015).
12. D. J. M. King, P. A. Burr, E. G. Obbard, and S. C. Middleburgh, Journal of Nuclear Materials **488**, 70 (2017).
13. P. Agrawal, S. Gupta, A. Dhal, R. Prabhakaran, L. Shao, and R. S. Mishra, Journal of Nuclear Materials **574**, 154217 (2023).
14. A. Kareer, J. C. Waite, B. Li, A. Couet, D. E. J. Armstrong, and A. J. Wilkinson, Journal of Nuclear Materials **526**, 151744 (2019).
15. B. Kombaiah, Y. Zhou, K. Jin, A. Manzoor, J. D. Poplawsky, J. A. Aguiar, H. Bei, D. S. Aidhy, P. D. Edmondson, and Y. Zhang, ACS Appl Mater Interfaces **15**, 3912 (2023).
16. B. Gwalani, S. Dasari, A. Sharma, V. Soni, S. Shukla, A. Jagetia, P. Agrawal, R. S. Mishra, and R. Banerjee, Acta Mater **219**, 117234 (2021).
17. Y. Zhao, Z. Chen, K. Yan, S. Naseem, W. Le, H. Zhang, and W. Lu, Materials Science and Engineering: A **838**, 142759 (2022).
18. S. Dasari, A. Jagetia, Y. J. Chang, V. Soni, B. Gwalani, S. Gorsse, A. C. Yeh, and R. Banerjee, J Alloys Compd **830**, 154707 (2020).
19. O. Oyelola, P. Crawforth, R. M'Saoubi, and A. T. Clare, Addit Manuf **24**, 20 (2018).
20. V. Chaudhary, N. M. Sai Kiran Kumar Yadav, S. A. Mantri, S. Dasari, A. Jagetia, R. V Ramanujan, and R. Banerjee, J Alloys Compd **823**, 153817 (2020).
21. W. Liu and J. N. DuPont, Scr Mater **48**, 1337 (2003).
22. D. D. Lima, S. A. Mantri, C. V Mikler, R. Contieri, C. J. Yannetta, K. N. Campo, E. S. Lopes, M. J. Styles, T. Borkar, R. Caram, and R. Banerjee, Mater Des **130**, 8 (2017).
23. M. S. K. K. Y. Nartu, A. Jagetia, V. Chaudhary, S. A. Mantri, E. Ivanov, N. B. Dahotre, R. V Ramanujan, and R. Banerjee, Scr Mater **187**, 30 (2020).
24. M. S. K. K. Y. Nartu, T. Alam, S. Dasari, S. A. Mantri, S. Gorsse, H. Siller, N. Dahotre, and R. Banerjee, Materialia (Oxf) **9**, 100522 (2020).
25. V. Chaudhary, M. S. K. K. Y. Nartu, S. Dasari, S. M. Varahabhatla, A. Sharma, M. Radhakrishnan, S. A. Mantri, S. Gorsse, N. B. Dahotre, R. V Ramanujan, and R. Banerjee, Scr Mater **224**, 115149 (2023).
26. M. S. K. K. Y. Nartu, D. Flannery, S. Mazumder, S. A. Mantri, S. S. Joshi, A. V. Ayyagari, B. McWilliams, K. Cho, N. B. Dahotre, and R. Banerjee, JOM 1 (2021).

27. M. S. K. K. Y. Nartu, S. Sharma, S. A. Mantri, S. S. Joshi, M. V. Pantawane, S. Mazumder, N. B. Dahotre, and R. Banerjee, in *Additive Manufacturing in Biomedical Applications* (ASM International, 2022), pp. 130–159.

28. M. S. K. K. Y. Nartu, A. Chesetti, S. Dasari, A. Sharma, S. A. Mantri, N. B. Dahotre, and R. Banerjee, Materials Science and Engineering: A **849**, 143505 (2022).

29. A. Chesetti, S. Banerjee, S. Dasari, S. M. Varahabhatla, A. Sharma, S. A. Mantri, M. S. K. K. Y. Nartu, N. Dahotre, and R. Banerjee, Additive Manufacturing Letters **6**, 100140 (2023).

30. C. Schneider-Maunoury, L. Weiss, P. Acquier, D. Boisselier, and P. Laheurte, Addit Manuf **17**, 55 (2017).

31. A. Gupta and M. Talha, Progress in Aerospace Sciences **79**, 1 (2015).

32. A. Sola, D. Bellucci, and V. Cannillo, Biotechnol Adv **34**, 504 (2016).

33. B. Saleh, J. Jiang, R. Fathi, T. Al-hababi, Q. Xu, L. Wang, D. Song, and A. Ma, Compos B Eng **201**, 108376 (2020).

34. V. Chaudhary, M. S. K. K. Y. Nartu, S. Dasari, S. M. Varahabhatla, A. Sharma, M. Radhakrishnan, S. A. Mantri, S. Gorsse, N. B. Dahotre, R. V. Ramanujan, and R. Banerjee, Scr Mater **224**, 115149 (2023).

35. M. Radhakrishnan, M. McKinstry, V. Chaudhary, M. S. K. K. Y. Nartu, K. V. M. Krishna, R. V. Ramanujan, R. Banerjee, and N. B. Dahotre, Scr Mater **226**, 115269 (2023).

36. X. Li, T. Wang, X. Ma, N. Overman, S. Whalen, D. Herling, and K. Kappagantula, J Manuf Process **80**, 108 (2022).

37. J. W. Yeh, S. K. Chen, S. J. Lin, J. Y. Gan, T. S. Chin, T. T. Shun, C. H. Tsau, and S. Y. Chang, Adv Eng Mater **6**, 299 (2004).

38. B. Gwalani, S. Gorsse, D. Choudhuri, Y. Zheng, R. S. Mishra, and R. Banerjee, Scr Mater **162**, 18 (2019).

39. S. Yadav, S. Sarkar, A. Aggarwal, A. Kumar, and K. Biswas, Wear **410–411**, 93 (2018).

40. K. R. Lim, K. S. Lee, J. S. Lee, J. Y. Kim, H. J. Chang, and Y. S. Na, J Alloys Compd **728**, 1235 (2017).

41. M. A. [Sandia N. Lab. (SNL-N. Melia Albuquerque, NM (United States)], J. D. [Sandia N. Lab. (SNL-N. Carroll Albuquerque, NM (United States)], S. R. [Sandia N. Lab. (SNL-N. Whetten Albuquerque, NM (United States)], S. N. [The O. S. Univ. Esmaeely Columbus, OH (United States)], J. [The O. S. Univ. Locke Columbus, OH (United States)], E. [Ames Lab. and I. S. Univ. White Ames, IA (United States)], I. [Ames Lab. and I. S. Univ. Anderson Ames, IA (United States)], M. [Sandia N. Lab. (SNL-N. Chandross Albuquerque, NM (United States)], J. R. [Sandia N. Lab. (SNL-N. Michael Albuquerque, NM (United States)], N. [Sandia N. Lab. (SNL-N. Argibay Albuquerque, NM (United States)], E. J. [Sandia N. Lab. (SNL-N. Schindelholz Albuquerque, NM (United States)], and A. B. [Sandia N. Lab. (SNL-N. Kustas Albuquerque, NM (United States)], (2019).

42. K. Kuwabara, H. Shiratori, T. Fujieda, K. Yamanaka, Y. Koizumi, and A. Chiba, Addit Manuf **23**, 264 (2018).

43. Y. Fan, Y. Zhang, H. Guan, H. Suo, and L. He, Rare Metal Materials and Engineering **42**, 1127 (2013).

44. V. Shivam, J. Basu, V. K. Pandey, Y. Shadangi, and N. K. Mukhopadhyay, Advanced Powder Technology **29**, 2221 (2018).

45. Z. Fu, W. Chen, H. Wen, Z. Chen, and E. J. Lavernia, J Alloys Compd **646**, 175 (2015).

46. C. Sun, P. Li, S. Xi, Y. Zhou, S. Li, and X. Yang, Materials Science and Engineering: A **728**, 144 (2018).

47. Z. Fu, W. Chen, H. Wen, D. Zhang, Z. Chen, B. Zheng, Y. Zhou, and E. J. Lavernia, Acta Mater **107**, 59 (2016).

48. Z. Tang, O. N. Senkov, C. M. Parish, C. Zhang, F. Zhang, L. J. Santodonato, G. Wang, G. Zhao, F. Yang, and P. K. Liaw, Materials Science and Engineering: A **647**, 229 (2015).

49. S. Mohanty, N. P. Gurao, P. Padaikathan, and K. Biswas, Mater Charact **129**, 127 (2017).

50. A. Emamifar, B. Sadeghi, P. Cavaliere, and H. Ziaei, Https://Doi.Org/10.1080/00325899.2019.1576389 **62**, 61 (2019).

51. N. Eißmann, B. Klöden, T. Weißgärber, and B. Kieback, Https://Doi.Org/10.1080/00325899.2017.1318480 **60**, 184 (2017).

52. A. I. Yurkova, V. V. Cherniavsky, V. Bolbut, M. Krüger, and I. Bogomol, J Alloys Compd **786**, 139 (2019).

53. P. Agrawal, R. S. Haridas, P. Agrawal, and R. S. Mishra, Addit Manuf **60**, 103282 (2022).

54. L. Hou, J. Hui, Y. Yao, J. Chen, and J. Liu, Vacuum **164**, 212 (2019).

55. S. Singh, N. Wanderka, B. S. Murty, U. Glatzel, and J. Banhart, Acta Mater **59**, 182 (2011).

56. Y. Liu, Y. Zhang, H. Zhang, N. Wang, X. Chen, H. Zhang, and Y. Li, J Alloys Compd **694**, 869 (2017).

57. D. G. Kim, Y. H. Jo, J. M. Park, W. M. Choi, H. S. Kim, B. J. Lee, S. S. Sohn, and S. Lee, J Alloys Compd **812**, 152111 (2020).

58. É. Fazakas, J. Q. Wang, V. Zadorozhnyy, D. V. Louzguine-Luzgin, and L. K. Varga, Materials and Corrosion **65**, 691 (2014).

59. Y. Du, Y. Lu, T. Wang, T. Li, and G. Zhang, Procedia Eng **27**, 1129 (2012).

60. Z. Yao, (2016).

61. S. qin Xia, Z. Wang, T. fei Yang, and Y. Zhang, Journal of Iron and Steel Research, International **22**, 879 (2015).

62. S. Q. Xia, X. Yang, T. F. Yang, S. Liu, and Y. Zhang, JOM **67**, 2340 (2015).

63. S. Shen, F. Chen, X. Tang, J. Lin, G. Ge, and J. Liu, Journal of Nuclear Materials **540**, 152380 (2020).

64. S. Xia, M. C. Gao, T. Yang, P. K. Liaw, and Y. Zhang, Journal of Nuclear Materials **480**, 100 (2016).

65. H. Zheng, R. Chen, G. Qin, X. Li, Y. Su, H. Ding, J. Guo, and H. Fu, J Alloys Compd **787**, 1023 (2019).

66. H. Zheng, R. Chen, G. Qin, X. Li, Y. Su, H. Ding, J. Guo, and H. Fu, J Mater Sci Technol **38**, 19 (2020).

67. S. T. Mileiko, S. A. Firstov, N. A. Novokhatskaya, V. F. Gorban, and N. P. Krapivka, Compos Part A Appl Sci Manuf **76**, 131 (2015).

68. Y. Yu, F. He, Z. Qiao, Z. Wang, W. Liu, and J. Yang, J Alloys Compd **775**, 1376 (2019).

69. F. He, Z. Wang, P. Cheng, Q. Wang, J. Li, Y. Dang, J. Wang, and C. T. Liu, J Alloys Compd **656**, 284 (2016).

70. S. Deepak Kumar, J. Ghose, and A. Mandal, Sustainable Engineering Products and Manufacturing Technologies 25 (2019).

71. G. T. Gray, V. Livescu, P. A. Rigg, C. P. Trujillo, C. M. Cady, S. R. Chen, J. S. Carpenter, T. J. Lienert, and S. J. Fensin, Acta Mater **138**, 140 (2017).

72. M. S. K. K. Y. Nartu, S. Dasari, A. Sharma, S. A. Mantri, S. Sharma, M. V. Pantawane, B. McWilliams, K. Cho, N. B. Dahotre, and R. Banerjee, Materials Science and Engineering: A **821**, 141627 (2021).

73. P. Wang, P. Huang, F. L. Ng, W. J. Sin, S. Lu, M. L. S. Nai, Z. L. Dong, and J. Wei, Mater Des **168**, 107576 (2019).

74. V. V. Popov, A. Katz-Demyanetz, A. Koptyug, and M. Bamberger, Heliyon **5**, e01188 (2019).

75. K. Kuwabara, H. Shiratori, T. Fujieda, K. Yamanaka, Y. Koizumi, and A. Chiba, Addit Manuf **23**, 264 (2018).

76. T. Fujieda, H. Shiratori, K. Kuwabara, M. Hirota, T. Kato, K. Yamanaka, Y. Koizumi, A. Chiba, and S. Watanabe, Mater Lett **189**, 148 (2017).

77. R. Li, P. Niu, T. Yuan, P. Cao, C. Chen, and K. Zhou, J Alloys Compd **746**, 125 (2018).

78. D. Lin, L. Xu, H. Jing, Y. Han, L. Zhao, and F. Minami, Addit Manuf **32**, 101058 (2020).

79. S. Luo, P. Gao, H. Yu, J. Yang, Z. Wang, and X. Zeng, J Alloys Compd **771**, 387 (2019).

80. X. Zhang, Y. Tong, Y. Hu, X. Liang, Y. Chen, K. Wang, M. Zhang, and J. Xu, Lubricants 2022, Vol. 10, Page 344 **10**, 344 (2022).

81. Md. R. U. Ahsan, G.-J. Seo, X. Fan, P. K. Liaw, S. Motaman, C. Haase, and D. B. Kim, J Manuf Process **68**, 1314 (2021).

82. K. A. Osintsev, S. V. Konovalov, V. E. Gromov, Y. F. Ivanov, and I. A. Panchenko, Mater Lett **312**, 131675 (2022).

83. D. K. Misra, C. Shang, T. Niendorf, K. Osintsev, S. Konovalov, D. Zaguliaev, Y. Ivanov, V. Gromov, and I. Panchenko, Metals 2022, Vol. 12, Page 197 **12**, 197 (2022).

84. C. S. Wu, P. H. Tsai, C. M. Kuo, and C. W. Tsai, Entropy 2018, Vol. 20, Page 967 **20**, 967 (2018).

85. P. Singh, A. Marshal, A. V. Smirnov, A. Sharma, G. Balasubramanian, K. G. Pradeep, and D. D. Johnson, Phys Rev Mater **3**, 075002 (2019).

86. S. M. Na, P. K. Lambert, H. Kim, J. Paglione, and N. J. Jones, AIP Adv **9**, 35010 (2019).

87. J. C. Rao, H. Y. Diao, V. Ocelík, D. Vainchtein, C. Zhang, C. Kuo, Z. Tang, W. Guo, J. D. Poplawsky, Y. Zhou, P. K. Liaw, and J. T. M. De Hosson, Acta Mater **131**, 206 (2017).

88. H. Y. Yasuda, K. Shigeno, and T. Nagase, Scr Mater **108**, 80 (2015).

89. F. Peyrouzet, D. Hachet, R. Soulas, C. Navone, S. Godet, and S. Gorsse, JOM **71**, 3443 (2019).

90. S. Dasari, A. Jagetia, Y. J. Chang, V. Soni, B. Gwalani, S. Gorsse, A. C. Yeh, and R. Banerjee, J Alloys Compd **830**, 154707 (2020).

91. L. Liu, P. Lazor, and X. Li, Https://Doi.Org/10.1080/08957959.2019.1653865 **39**, 533 (2019).

92. M. V. Karpets, O. S. Makarenko, V. F. Gorban', M. O. Krapivka, O. A. Rokitska, and S. Y. Makarenko, Powder Metallurgy and Metal Ceramics **55**, 361 (2016).

93. N. Zhou, S. Jiang, T. Huang, M. Qin, T. Hu, and J. Luo, Sci Bull (Beijing) **64**, 856 (2019).

94. P. K. Sarswat, S. Sarkar, A. Murali, W. Huang, W. Tan, and M. L. Free, Appl Surf Sci **476**, 242 (2019).

95. Z. Wang, I. Baker, Z. Cai, S. Chen, J. D. Poplawsky, and W. Guo, Acta Mater **120**, 228 (2016).

96. N. Liu, C. Chen, I. Chang, P. Zhou, and X. Wang, Materials 2018, Vol. 11, Page 1290 **11**, 1290 (2018).

97. P. Singh, A. Marshal, A. V. Smirnov, A. Sharma, G. Balasubramanian, K. G. Pradeep, and D. D. Johnson, Phys Rev Mater **3**, 075002 (2019).

98. P. Asghari-Rad, P. Sathiyamoorthi, J. W. Bae, J. Moon, J. M. Park, A. Zargaran, and H. S. Kim, Materials Science and Engineering: A **744**, 610 (2019).

99. Q. Ding, Y. Zhang, X. Chen, X. Fu, D. Chen, S. Chen, L. Gu, F. Wei, H. Bei, Y. Gao, M. Wen, J. Li, Z. Zhang, T. Zhu, R. O. Ritchie, and Q. Yu, Nature 2019 574:7777 **574**, 223 (2019).

100. K. Guruvidyathri, B. S. Murty, J. W. Yeh, and K. C. Hari Kumar, J Alloys Compd **768**, 358 (2018).

101. D. G. Kim, Y. H. Jo, J. M. Park, W. M. Choi, H. S. Kim, B. J. Lee, S. S. Sohn, and S. Lee, J Alloys Compd **812**, 152111 (2020).

102. Z. Wu, H. Bei, F. Otto, G. M. Pharr, and E. P. George, Intermetallics (Barking) **46**, 131 (2014).

103. S. Sohn, Y. Liu, J. Liu, P. Gong, S. Prades-Rodel, A. Blatter, B. E. Scanley, C. C. Broadbridge, and J. Schroers, Scr Mater **126**, 29 (2017).

104. T. Nagase, A. Shibata, M. Matsumuro, M. Takemura, and S. Semboshi, Mater Des **181**, 107900 (2019).

105. K. Sarlar, A. Tekgül, and I. Kucuk, Current Applied Physics **20**, 18 (2020).

106. S. Gou, M. Gao, Y. Shi, S. Li, Y. Fang, X. Chen, H. Chen, W. Yin, J. Liu, Z. Lei, and H. Wang, Acta Mater **248**, 118781 (2023).

107. V. T. Nguyen, M. Qian, Z. Shi, T. Song, L. Huang, and J. Zou, Materials Science and Engineering: A **742**, 762 (2019).

108. Y. Yuan, Y. Wu, X. Tong, H. Zhang, H. Wang, X. J. Liu, L. Ma, H. L. Suo, and Z. P. Lu, Acta Mater **125**, 481 (2017).

109. J. W. Qiao, M. L. Bao, Y. J. Zhao, H. J. Yang, Y. C. Wu, Y. Zhang, J. A. Hawk, and M. C. Gao, J Appl Phys **124**, 195101 (2018).

110. M. Feuerbacher, M. Heidelmann, and C. Thomas, Http://Mc.Manuscriptcentral.Com/Tmrl **3**, 1 (2015).

111. A. Takeuchi, K. Amiya, T. Wada, K. Yubuta, and W. Zhang, JOM **66**, 1984 (2014).

112. J. W. Qiao, M. L. Bao, Y. J. Zhao, H. J. Yang, Y. C. Wu, Y. Zhang, J. A. Hawk, and M. C. Gao, J Appl Phys **124**, 195101 (2018).

113. Y. J. Zhao, J. W. Qiao, S. G. Ma, M. C. Gao, H. J. Yang, M. W. Chen, and Y. Zhang, Mater Des **96**, 10 (2016).

114. S. Y. Chen, X. Yang, K. A. Dahmen, P. K. Liaw, and Y. Zhang, Entropy 2014, Vol. 16, Pages 870-884 **16**, 870 (2014).

115. O. N. Senkov, S. V. Senkova, and C. Woodward, Acta Mater **68**, 214 (2014).

116. D. D. Zhang, J. Y. Zhang, J. Kuang, G. Liu, and J. Sun, Acta Mater **220**, 117288 (2021).

117. O. N. Senkov, S. V. Senkova, D. B. Miracle, and C. Woodward, Materials Science and Engineering: A **565**, 51 (2013).

118. H. Chen, A. Kauffmann, S. Seils, T. Boll, C. H. Liebscher, I. Harding, K. S. Kumar, D. V. Szabó, S. Schlabach, S. Kauffmann-Weiss, F. Müller, B. Gorr, H. J. Christ, and M. Heilmaier, Acta Mater **176**, 123 (2019).

119. Y. Wu, J. Si, D. Lin, T. Wang, W. Y. Wang, Y. Wang, Z. K. Liu, and X. Hui, Materials Science and Engineering: A **724**, 249 (2018).

120. O. N. Senkov, C. Woodward, and D. B. Miracle, JOM **66**, 2030 (2014).

121. P. Lu, J. E. Saal, G. B. Olson, T. Li, O. J. Swanson, G. S. Frankel, A. Y. Gerard, K. F. Quiambao, and J. R. Scully, Scr Mater **153**, 19 (2018).

122. A. Raturi, J. Aditya C, N. P. Gurao, and K. Biswas, J Alloys Compd **806**, 587 (2019).

123. Y. Lu, H. Huang, X. Gao, C. Ren, J. Gao, H. Zhang, S. Zheng, Q. Jin, Y. Zhao, C. Lu, T. Wang, and T. Li, J Mater Sci Technol **35**, 369 (2019).

124. S. Marik, K. Motla, M. Varghese, K. P. Sajilesh, D. Singh, Y. Breard, P. Boullay, and R. P. Singh, Phys Rev Mater **3**, 060602 (2019).

125. S. Marik, M. Varghese, K. P. Sajilesh, D. Singh, and R. P. Singh, J Alloys Compd **769**, 1059 (2018).

126. Y. S. Lee and R. J. Cava, Physica C: Superconductivity and Its Applications **566**, 1353520 (2019).

127. J. Moon, J. M. Park, J. W. Bae, H. S. Do, B. J. Lee, and H. S. Kim, Acta Mater **193**, 71 (2020).

128. S. Son, J. Moon, H. Kwon, P. Asghari Rad, H. Kato, and H. S. Kim, Metals 2021, Vol. 11, Page 238 **11**, 238 (2021).

129. K. B. Zhang, Z. Y. Fu, J. Y. Zhang, J. Shi, W. M. Wang, H. Wang, Y. C. Wang, and Q. J. Zhang, J Alloys Compd **502**, 295 (2010).

130. M. H. Tsai, H. Yuan, G. Cheng, W. Xu, W. W. Jian, M. H. Chuang, C. C. Juan, A. C. Yeh, S. J. Lin, and Y. Zhu, Intermetallics (Barking) **33**, 81 (2013).

131. E. Jumaev, S. H. Hong, J. T. Kim, H. J. Park, Y. S. Kim, S. C. Mun, J. Y. Park, G. Song, J. K. Lee, B. H. Min, T. Lee, and K. B. Kim, J Alloys Compd **777**, 828 (2019).

132. P. Edalati, A. Mohammadi, M. Ketabchi, and K. Edalati, J Alloys Compd **884**, 161101 (2021).

133. K. Baba, N. Ishizu, T. Nishizaki, and J. Kitagawa, Materials 2021, Vol. 14, Page 2877 **14**, 2877 (2021).

134. Z. Tang, T. Yuan, C. W. Tsai, J. W. Yeh, C. D. Lundin, and P. K. Liaw, Acta Mater **99**, 247 (2015).

135. Z. Li and D. Raabe, Mater Chem Phys **210**, 29 (2018).

136. Q. Wang, L. Zeng, T. Gao, H. Du, and X. Liu, J Mater Sci Technol **87**, 29 (2021).
137. H. Ren, R. R. Chen, X. F. Gao, T. Liu, G. Qin, S. P. Wu, and J. J. Guo, J Alloys Compd **929**, 167374 (2022).
138. C. W. Lu, Y. S. Lu, Z. H. Lai, H. W. Yen, and Y. L. Lee, J Alloys Compd **842**, 155824 (2020).
139. S. Shuang, Y. Liang, C. Yu, al -, C. Huang, Y. Yao, and X. Peng, J Electrochem Soc **167**, 081506 (2020).
140. G. Perumal, H. S. Grewal, M. Pole, L. V. K. Reddy, S. Mukherjee, H. Singh, G. Manivasagam, and H. S. Arora, ACS Appl Bio Mater **3**, 1233 (2020).
141. Y. P. Cai, G. J. Wang, Y. J. Ma, Z. H. Cao, and X. K. Meng, Scr Mater **162**, 281 (2019).
142. P. Cui, Z. Bao, Y. Liu, F. Zhou, Z. Lai, Y. Zhou, and J. Zhu, Corros Sci **201**, 110276 (2022).
143. S. Xia, Z. Xia, D. Zhao, Y. Xie, X. Liu, and L. Wang, Fusion Engineering and Design **172**, 112792 (2021).
144. P. Edalati, A. Mohammadi, M. Ketabchi, and K. Edalati, J Alloys Compd **894**, 162413 (2022).
145. S. Sun, H. Liu, J. Hao, and H. Yang, J Alloys Compd **886**, 161251 (2021).
146. K. Patel, V. Hasannaeimi, M. Sadeghilaridjani, S. Muskeri, C. Mahajan, and S. Mukherjee, Entropy 2023, Vol. 25, Page 296 **25**, 296 (2023).
147. Y. Liu, J. Tu, C. hao Wang, J. ru Luo, L. peng Ding, P. huai Wang, and Z. ming Zhou, J Alloys Compd **858**, 157642 (2021).
148. P. Fu, H. Su, Z. Li, P. Dai, and Q. Tang, J Alloys Compd **921**, 166141 (2022).
149. S. S. Nene, K. Liu, S. Sinha, M. Frank, S. Williams, and R. S. Mishra, Materialia (Oxf) **9**, 100521 (2020).
150. S. Luo, C. Zhao, Y. Su, Q. Liu, and Z. Wang, Addit Manuf **31**, 100925 (2020).
151. L. Gu, N. Liang, Y. Liu, Y. Chen, J. Liu, Y. Sun, and Y. Zhao, Mater Lett **324**, 132676 (2022).
152. D. G. Shaysultanov, G. A. Salishchev, Y. V. Ivanisenko, S. V. Zherebtsov, M. A. Tikhonovsky, and N. D. Stepanov, J Alloys Compd **705**, 756 (2017).
153. H. Ren, R. R. Chen, X. F. Gao, T. Liu, G. Qin, S. P. Wu, and J. J. Guo, Materials Science and Engineering: A **862**, 144425 (2023).
154. O. N. Senkov, C. Woodward, and D. B. Miracle, JOM **66**, 2030 (2014).
155. B. Gwalani, S. Dasari, A. Sharma, V. Soni, S. Shukla, A. Jagetia, P. Agrawal, R. S. Mishra, and R. Banerjee, Acta Mater **219**, 117234 (2021).
156. A. Chesetti, S. Banerjee, S. Dasari, M. S. K. Nartu, S. M. Varahabhatla, A. Sharma, A. Ramakrishnan, D. Satko, S. Gorsse, A. Salem, and R. Banerjee, Scr Mater **225**, 115160 (2023).
157. K. Ming, X. Bi, and J. Wang, Int J Plast **100**, 177 (2018).
158. S. G. Ma and Y. Zhang, Materials Science and Engineering: A **532**, 480 (2012).
159. S. Dasari, A. Jagetia, Y. J. Chang, V. Soni, B. Gwalani, S. Gorsse, A. C. Yeh, and R. Banerjee, J Alloys Compd **830**, 154707 (2020).
160. S. Shukla, D. Choudhuri, T. Wang, K. Liu, R. Wheeler, S. Williams, B. Gwalani, and R. S. Mishra, Mater Res Lett **6**, 676 (2018).
161. Y. L. Zhao, T. Yang, Y. R. Li, L. Fan, B. Han, Z. B. Jiao, D. Chen, C. T. Liu, and J. J. Kai, Acta Mater **188**, 517 (2020).
162. K. Zhang, H. Wen, B. Zhao, X. Dong, and L. Zhang, Mater Charact **155**, 109792 (2019).
163. J. Peng, Z. Li, L. Fu, X. Ji, Z. Pang, and A. Shan, J Alloys Compd **803**, 491 (2019).
164. N. Gao, D. H. Lu, Y. Y. Zhao, X. W. Liu, G. H. Liu, Y. Wu, G. Liu, Z. T. Fan, Z. P. Lu, and E. P. George, J Alloys Compd **792**, 1028 (2019).
165. H. Cheng, W. Chen, X. Liu, Q. Tang, Y. Xie, and P. Dai, Materials Science and Engineering: A **719**, 192 (2018).
166. J. Chen, Z. Yao, X. Wang, Y. Lu, X. Wang, Y. Liu, and X. Fan, Mater Chem Phys **210**, 136 (2018).

167. L. B. Chen, R. Wei, K. Tang, J. Zhang, F. Jiang, L. He, and J. Sun, Materials Science and Engineering: A **716**, 150 (2018).

168. J. Y. Ko and S. I. Hong, J Alloys Compd **743**, 115 (2018).

169. Z. Li, Acta Mater **164**, 400 (2019).

170. L. Guo, X. Ou, S. Ni, Y. Liu, and M. Song, Materials Science and Engineering: A **746**, 356 (2019).

171. Z. Wang, I. Baker, W. Guo, and J. D. Poplawsky, Acta Mater **126**, 346 (2017).

172. Y. Ma, X. Liu, W. Dong, R. Li, Y. Zhang, Y. Lu, P. Yu, and G. Li, Materials Science and Engineering: A **792**, 139802 (2020).

173. R. Li, D. Kong, K. He, and C. Dong, Scr Mater **230**, 115401 (2023).

174. Y. L. Wang, L. Zhao, D. Wan, S. Guan, and K. C. Chan, Materials Science and Engineering: A **825**, 141871 (2021).

175. T. Fujieda, M. Chen, H. Shiratori, K. Kuwabara, K. Yamanaka, Y. Koizumi, A. Chiba, and S. Watanabe, Addit Manuf **25**, 412 (2019).

176. S. Gou, M. Gao, Y. Shi, S. Li, Y. Fang, X. Chen, H. Chen, W. Yin, J. Liu, Z. Lei, and H. Wang, Acta Mater **248**, 118781 (2023).

177. Y. K. Kim, K. Ram Lim, and K. A. Lee, Mater Des **227**, 111761 (2023).

178. T. M. Smith, C. A. Kantzos, N. A. Zarkevich, B. J. Harder, M. Heczko, P. R. Gradl, A. C. Thompson, M. J. Mills, T. P. Gabb, and J. W. Lawson, Nature 2023 617:7961 **617**, 513 (2023).

179. T. M. Smith, A. C. Thompson, T. P. Gabb, C. L. Bowman, and C. A. Kantzos, Scientific Reports 2020 10:1 **10**, 1 (2020).

180. J. Su, D. Raabe, and Z. Li, Acta Mater **163**, 40 (2019).

181. D. Wei, X. Li, J. Jiang, W. Heng, Y. Koizumi, W. M. Choi, B. J. Lee, H. S. Kim, H. Kato, and A. Chiba, Scr Mater **165**, 39 (2019).

182. Z. Yang, D. Yan, W. Lu, and Z. Li, Materials Science and Engineering: A **801**, 140441 (2021).

183. X. Wu, D. Mayweg, D. Ponge, and Z. Li, Materials Science and Engineering: A **802**, 140661 (2021).

184. R. Wei, K. Zhang, L. Chen, Z. Han, T. Wang, C. Chen, J. Jiang, T. Hu, and F. Li, J Mater Sci Technol **57**, 153 (2020).

185. D. D. Zhang, J. Y. Zhang, J. Kuang, G. Liu, and J. Sun, Acta Mater **220**, 117288 (2021).

186. Z. Li, C. C. Tasan, K. G. Pradeep, and D. Raabe, Acta Mater **131**, 323 (2017).

187. S. Chen, H. S. Oh, B. Gludovatz, S. J. Kim, E. S. Park, Z. Zhang, R. O. Ritchie, and Q. Yu, Nature Communications 2020 11:1 **11**, 1 (2020).

188. Y. Jung, K. Lee, S. J. Hong, J. K. Lee, J. Han, K. B. Kim, P. K. Liaw, C. Lee, and G. Song, J Alloys Compd **886**, 161187 (2021).

189. S. Lee, G. Choi, and K. Lee, Int J Refract Metals Hard Mater **100**, 105628 (2021).

190. L. Lilensten, J. P. Couzinié, J. Bourgon, L. Perrière, G. Dirras, F. Prima, and I. Guillot, Mater Res Lett **5**, 110 (2017).

191. L. Wang, C. Fu, Y. Wu, Q. Wang, X. Hui, and Y. Wang, Materials Science and Engineering: A **748**, 441 (2019).

192. V. T. Nguyen, M. Qian, Z. Shi, T. Song, L. Huang, and J. Zou, Materials Science and Engineering: A **742**, 762 (2019).

193. L. Wang, C. Fu, Y. Wu, R. Li, Y. Wang, and X. Hui, Materials Science and Engineering: A **763**, 138147 (2019).

194. P. Agrawal, S. Gupta, A. Dhal, R. Prabhakaran, L. Shao, and R. S. Mishra, Journal of Nuclear Materials **574**, 154217 (2023).

195. X. Xian, Z. Zhong, B. Zhang, K. Song, C. Chen, S. Wang, J. Cheng, and Y. Wu, Mater Des **121**, 229 (2017).

196. O. A. Waseem and H. J. Ryu, Scientific Reports 2017 7:1 **7**, 1 (2017).

197. A. Kareer, J. C. Waite, B. Li, A. Couet, D. E. J. Armstrong, and A. J. Wilkinson, Journal of Nuclear Materials **526**, 151744 (2019).
198. F. Granberg, K. Nordlund, M. W. Ullah, K. Jin, C. Lu, H. Bei, L. M. Wang, F. Djurabekova, W. J. Weber, and Y. Zhang, Phys Rev Lett **116**, 135504 (2016).
199. S. Q. Xia, X. Yang, T. F. Yang, S. Liu, and Y. Zhang, JOM **67**, 2340 (2015).
200. T. Egami, W. Guo, P. D. Rack, and T. Nagase, Metall Mater Trans A Phys Metall Mater Sci **45**, 180 (2014).
201. M. Sadeghilaridjani, A. Ayyagari, S. Muskeri, V. Hasannaeimi, R. Salloom, W. Y. Chen, and S. Mukherjee, Journal of Nuclear Materials **529**, 151955 (2020).
202. O. El-Atwani, N. Li, M. Li, A. Devaraj, J. K. S. Baldwin, M. M. Schneider, D. Sobieraj, J. S. Wróbel, D. Nguyen-Manh, S. A. Maloy, and E. Martinez, Sci Adv **5**, (2019).
203. R. Li, D. Kong, K. He, and C. Dong, Scr Mater **230**, 115401 (2023).
204. D. J. M. King, S. T. Y. Cheung, S. A. Humphry-Baker, C. Parkin, A. Couet, M. B. Cortie, G. R. Lumpkin, S. C. Middleburgh, and A. J. Knowles, Acta Mater **166**, 435 (2019).
205. C. Xiang, E. H. Han, Z. M. Zhang, H. M. Fu, J. Q. Wang, H. F. Zhang, and G. D. Hu, Intermetallics (Barking) **104**, 143 (2019).
206. Y. Lu, H. Huang, X. Gao, C. Ren, J. Gao, H. Zhang, S. Zheng, Q. Jin, Y. Zhao, C. Lu, T. Wang, and T. Li, J Mater Sci Technol **35**, 369 (2019).
207. Y. Zong, N. Hashimoto, and H. Oka, Nuclear Materials and Energy **31**, 101158 (2022).
208. C. Xiang, H. M. Fu, Z. M. Zhang, E. H. Han, H. F. Zhang, J. Q. Wang, and G. D. Hu, J Alloys Compd **818**, 153352 (2020).
209. D. Li, Y. Dong, Z. Zhang, Q. Zhang, S. Chen, N. Jia, H. Wang, B. Wang, K. Jin, Y. Xue, Y. Dou, X. He, W. Yang, L. Wang, and H. Cai, J Alloys Compd **877**, 160199 (2021).
210. K. K. Tseng, Y. C. Yang, C. C. Juan, T. S. Chin, C. W. Tsai, and J. W. Yeh, Sci China Technol Sci **61**, 184 (2018).
211. O. El Atwani, H. T. Vo, M. A. Tunes, C. Lee, A. Alvarado, N. Krienke, J. D. Poplawsky, A. A. Kohnert, J. Gigax, W. Y. Chen, M. Li, Y. Q. Wang, J. S. Wróbel, D. Nguyen-Manh, J. K. S. Baldwin, O. U. Tukac, E. Aydogan, S. Fensin, and E. Martinez, Nature Communications 2023 14:1 **14**, 1 (2023).
212. Y. Ma, Y. Zhang, Z. Zhang, L. Liu, and L. Sun, Intermetallics (Barking) **157**, 107872 (2023).
213. Y. Wang, S. Li, F. Chen, K. Yang, G. Ge, X. Tang, M. Fan, and P. Huang, J Alloys Compd **958**, 170373 (2023).
214. R. Martins, J. B. Correia, P. Czarkowski, R. Miklaszewski, A. Malaquias, R. Mateus, E. Alves, and M. Dias, Nucl Instrum Methods Phys Res B **538**, 212 (2023).
215. A. Hussain, S. A. Khan, S. K. Sharma, K. Sudarshan, S. K. Sharma, C. Singh, and P. K. Kulriya, Materials Science and Engineering: A **863**, 144523 (2023).
216. M. A. Tunes, S. Fritze, B. Osinger, P. Willenshofer, A. M. Alvarado, E. Martinez, A. S. Menon, P. Ström, G. Greaves, E. Lewin, U. Jansson, S. Pogatscher, T. A. Saleh, V. M. Vishnyakov, and O. El-Atwani, Acta Mater **250**, 118856 (2023).
217. J. Liu, X. An, J. Zhang, Q. Kong, Q. Li, H. Wang, W. Yao, and Q. Wang, Intermetallics (Barking) **153**, 107775 (2023).
218. O. N. Senkov, G. B. Wilks, J. M. Scott, and D. B. Miracle, Intermetallics (Barking) **19**, 698 (2011).
219. M. S. K. K. Y. Nartu, A. Chesetti, S. Dasari, A. Sharma, S. A. Mantri, N. B. Dahotre, and R. Banerjee, Materials Science and Engineering A **849**, (2022).
220. Mohan Sai Kiran Kumar Yadav Nartu, Shristy Jha, Advika Chesetti, Sundeep Mukherjee, Isabella Van Rooyen, and Rajarshi Banerjee, JOM (2023).
221. V. Kumar, A. Gupta, D. Lahiri, and K. Balani, J Phys D Appl Phys **46**, (2013).
222. C. A. Schuh, Materials Today **9**, 32 (2006).
223. J. Il Jang, M. J. Lance, S. Wen, T. Y. Tsui, and G. M. Pharr, Acta Mater **53**, 1759 (2005).
224. S. Banerjee and U. M. Naik, Acta Mater **44**, 3667 (1996).

225. D. Choudhuri, S. A. Mantri, T. Alam, S. Banerjee, and R. Banerjee, Scr Mater **124**, 15 (2016).

226. C. Downey, Development of Advanced Coating Technologies Using Powder-Blown Directed Energy Deposition (DED) Additive Manufacturing for Advanced Nuclear Reactor Applications , Master's Thesis, University of Idaho, 2023.

227. C. Downey, L. Nunez, J. Toman, M. Abdo, and I.J. van Rooyen TMS 2023 Conference Presentation, (2023).

228. C. Downey, I.J. Van Rooyen, L. Nunez - US Patent App. 18/069,023, 2023.

**Pacific Northwest
National Laboratory**

902 Battelle Boulevard
P.O. Box 999
Richland, WA 99354
1-888-375-PNNL (7665)

www.pnnl.gov